

# Magnetic acceleration of relativistic AGN jets

Serguei S. Komissarov,<sup>1\*</sup> Maxim V. Barkov,<sup>1,2\*</sup> Nektarios Vlahakis<sup>3\*</sup> and ArieH Königl<sup>4\*</sup>

<sup>1</sup>*Department of Applied Mathematics, The University of Leeds, Leeds, LS2 9GT*

<sup>2</sup>*Space Research Institute, 84/32 Profsoyuznaya Street, Moscow 117997, Russia*

<sup>3</sup>*Section of Astrophysics, Astronomy and Mechanics, Physics Department, University of Athens, 15784 Zografos, Athens, Greece*

<sup>4</sup>*Department of Astronomy and Astrophysics and Enrico Fermi Institute, University of Chicago, 5640 South Ellis Avenue, Chicago, IL 60637, USA*

Received/Accepted

## ABSTRACT

We present numerical simulations of axisymmetric, magnetically driven relativistic jets. Our special-relativistic, ideal-MHD numerical scheme is specifically designed to optimize accuracy and resolution and to minimize numerical dissipation. In addition, we implement a grid-extension method that reduces the computation time by up to three orders of magnitude and makes it possible to follow the flow up to six decades in spatial scale. To eliminate the dissipative effects induced by a free boundary with an ambient medium we assume that the flow is confined by a rigid wall of a prescribed shape, which we take to be  $z \propto r^a$  (in cylindrical coordinates, with  $a$  ranging from 1 to 3). We also prescribe, through the rotation profile at the inlet boundary, the injected poloidal current distribution: we explore cases where the return current flows either within the volume of the jet or on the outer boundary. The outflows are initially cold, sub-Alfvénic and Poynting flux-dominated, with a total-to-rest-mass energy flux ratio  $\mu \sim 15$ . We find that in all cases they converge to a steady state characterized by a spatially extended acceleration region. The acceleration process is very efficient: on the outermost scale of the simulation as much as  $\sim 77\%$  of the Poynting flux has been converted into kinetic energy flux, and the terminal Lorentz factor approaches its maximum possible value ( $\Gamma_\infty \simeq \mu$ ). We also find a high collimation efficiency: all our simulated jets (including the limiting case of an unconfined flow) develop a cylindrical core. We argue that this could be the rule for current-carrying outflows that start with a low initial Lorentz factor ( $\Gamma_0 \sim 1$ ). Our conclusions on the high acceleration and collimation efficiencies are not sensitive to the particular shape of the confining boundary or to the details of the injected current distribution, and they are qualitatively consistent with the semi-analytic self-similar solutions derived by Vlahakis & Königl. We apply our results to the interpretation of relativistic jets in AGNs: we argue that they naturally account for the spatially extended accelerations inferred in these sources ( $\Gamma_\infty \gtrsim 10$  attained on radial scales  $R \gtrsim 10^{17}$  cm) and are consistent with the transition to the matter-dominated regime occurring already at  $R \gtrsim 10^{16}$  cm.

**Key words:** galaxies: active – galaxies: jets – methods: numerical – MHD – relativity

## 1 INTRODUCTION

There is strong evidence for relativistic motions in jets that emanate from active galactic nuclei (AGNs). In particular, apparent superluminal speeds  $\beta_{\text{app}}$  (in units of the speed of light  $c$ ) as high as  $\sim 40$  have been measured for radio components on (projected) scales of  $\sim 1 - 10$  pc in the blazar class

of sources (e.g. Jorstad et al. 2001). Jorstad et al. (2005) used a method based on a comparison between the time scale of flux density decline and the light-travel time across the imaged emission region to relate  $\beta_{\text{app}}$  to the bulk Lorentz factor  $\Gamma$  of the outflow; they inferred that the Lorentz factors of blazar jets lie in the range  $\sim 5 - 40$ , with the majority of quasar components having  $\Gamma \sim 16 - 18$  and with BL Lac objects possessing a more uniform  $\Gamma$  distribution. Cohen et al. (2007) recently reached a similar conclusion on the basis of probability arguments, inferring that roughly half the sources in a flux density-limited, beamed sample

\* E-Mail: serguei@maths.leeds.ac.uk (SSK);  
bmv@maths.leeds.ac.uk (MVB); vlahakis@phys.uoa.gr (NV);  
arieh@jets.uchicago.edu (AK)

have a value of  $\Gamma$  close to the measured  $\beta_{\text{app}}$ . They further deduced that the maximum Lorentz factor in their sample of 119 AGN jets is  $\sim 32$ , close to the value of  $\sim 40$  inferred for the jets observed by Jorstad et al. (2001, 2005).

The presence of relativistic bulk motions in blazar jets has been independently indicated by measurements of rapid variations in the total and polarized fluxes (e.g. Hartman et al. 2001; Rebillot et al. 2006; Bach et al. 2006; Villata et al. 2006). There is also evidence that the relativistic speeds persist to large scales. For example, apparent superluminal component motions have been measured in the 3C 120 jet out to projected distances from the source of at least 150 pc (Walker et al. 2001), and it has been argued that the spectral properties of the heads of extended (up to several hundred kiloparsecs) jets can be explained in the context of a relativistic flow that is decelerated to subrelativistic speeds at the termination shock that advances into the ambient medium (Georganopoulos & Kazanas 2003).

The main source of power of AGN jets is the rotational energy of the central supermassive black hole (e.g. Lovelace 1976; Blandford & Znajek 1977) and/or its accretion disk (e.g. Blandford 1976). The naturally occurring low mass density and hence high magnetization of black-hole magnetospheres suggests that the relativistic jets originate directly from the black-hole ergosphere, whereas the disk surface launches a slower, possibly nonrelativistic wind that surrounds and confines the highly relativistic flow. This picture finds support in recent numerical simulations (e.g. McKinney & Gammie 2004; De Villiers et al. 2005). However, this issue is far from settled and one cannot rule out the inner part of accretion disk as a base of a relativistic outflow (e.g. Vlahakis & Königl 2004). The theory of relativistic, magnetically driven jets from black holes (and neutron stars) predicts highly magnetized flows, with the Poynting flux dominating the total energy output. At the jet emission site this energy has to be transferred to particles. This transfer may have the form of magnetic dissipation (e.g. Blandford 2002; Lyutikov & Blandford 2003) but the still commonly held view is that the Poynting energy is first converted into bulk kinetic energy and only subsequently channeled into radiation through shocks and other dissipative waves (e.g. Blandford & Rees 1974; Begelman et al. 1984). The jet radiative efficiency is still one of the key debatable issues in the theory of Poynting-dominated outflows. In principle, slow magnetic dissipation in an expanding jet may also facilitate the gradual conversion of Poynting flux into bulk kinetic energy (Drenkhahn & Spruit 2002).

When the inertia of the plasma is negligibly small its dynamics is well described by the approximation of force-free electrodynamics (or magnetodynamics; e.g. Komissarov 2002; Komissarov, Barkov & Lyutikov 2007). The equations of magnetodynamics are much simpler than those of magnetohydrodynamics (MHD), which is what prompted their application to the study of the magnetic acceleration of relativistic jets (e.g. Blandford 1976, 2002; Narayan, McKinney & Farmer 2007). The solutions of these equations describe trans-Alfvénic flows whose drift velocity approaches the speed of light at infinity, the location of the fast critical point in these models. However, within this framework it is impossible to account for the conversion of Poynting flux into plasma kinetic energy and to study the issue of the acceleration efficiency.

The next simplest approximation that can be used to address the issue of Poynting-to-kinetic energy conversion is ideal MHD. In this case one can obtain exact semi-analytic solutions, although, because of the complexity of the problem, this can only be done when the system possesses a high degree of symmetry. This approach was pioneered by Blandford & Payne (1982), who constructed non-relativistic semi-analytic solutions for steady-state, cold, self-similar (in the spherical radial coordinate) disk outflows. These solutions were generalized to the (special) relativistic MHD regime by Li, Chiueh & Begelman (1992) and by Contopoulos (1994). They were further investigated by Vlahakis & Königl (2003a,b), who also considered the effect of thermal forces during the early phases of the acceleration.<sup>1</sup> Solutions with similar properties were derived in Beskin & Nokhrina (2006) by linearizing about a force-free solution for a paraboloidal field geometry.

A key property of the relativistic solutions derived in the aforementioned studies is the extended nature of the acceleration region: the bulk of the (poloidal) acceleration is effected by magnetic pressure gradients (associated with the azimuthal magnetic field component) and takes place beyond the classical fast-magnetosonic point (a singular point of the Bernoulli equation). Vlahakis & Königl (2003a) interpreted this behaviour (which was dubbed the “magnetic nozzle” effect by Li et al. 1992; see also Camenzind 1989) in terms of the distinction between the classical and the modified fast-magnetosonic surfaces (e.g. Bogovalov 1997). They pointed out that the latter surface, which is the locus of the fast-magnetosonic singular points of the combined Bernoulli and trans-field (or Grad-Shafranov) equations, is the true causality surface (or “event horizon”) for the propagation of fast waves when the shape of the field lines is obtained from the solution of the trans-field equation (with the classical surface playing this role only when the shape of the flux surfaces is predetermined). They argued that, in this case, the acceleration continues all the way to (and possibly even past) the modified fast-magnetosonic surface, which can lie well beyond the classical one.<sup>2</sup> Another general property of the cold MHD solutions is that, in the current-carrying regime (where the poloidal components of the current density and the magnetic field are antiparallel) they collimate (asymptotically) to cylinders. Furthermore, the asymptotic Lorentz factor corresponds to a rough equipartition between the Poynting and kinetic energy fluxes.

The continuation of the acceleration process beyond the classical fast-magnetosonic surface is evidently a general characteristic of steady-state MHD solutions that applies also to nonrelativistic jets (e.g. Vlahakis et al. 2000). This behaviour should, however, be more clearly discerned in observations of relativistic flows, where the proper speed

<sup>1</sup> Vlahakis & Königl (2003a) focused on flows whose initial poloidal velocity component is sub-Alfvénic, corresponding to the poloidal magnetic field component dominating the azimuthal field component at the top of the disk, whereas Vlahakis & Königl (2003b) discussed the super-Alfvénic case in which the azimuthal component is dominant at the base of the flow. In this paper we only consider outflows of the first type.

<sup>2</sup> In the radially self-similar solutions presented in Vlahakis & Königl (2003a), the modified fast-magnetosonic surface formally lies at an infinite distance from the origin.

$\Gamma\beta$  can increase by a large factor between the classical and the modified singular surfaces. In contrast, the magnetic acceleration of non-relativistic flows is almost complete at the classical fast point. This striking difference has a very simple origin. For nonrelativistic flows the criticality condition at the classical fast-magnetosonic point implies equipartition between the magnetic energy and the kinetic energy of poloidal motion. The kinetic energy can therefore increase by at most a factor of 2 beyond this point. However, relativistic flows remain magnetically dominated at the fast-magnetosonic point, which means that there is an ample remaining supply of magnetic energy that can be used for flow acceleration downstream of this point (e.g. Komissarov 2004).

In the case of AGNs there have indeed been indications from a growing body of data that the associated relativistic jets undergo the bulk of their acceleration on scales that are of the order of those probed by very-long-baseline radio interferometry. In one line of reasoning, the absence of bulk-Comptonization spectral signatures in blazars has been used to infer that jet Lorentz factors  $\gtrsim 10$  are only attained on scales  $\gtrsim 10^{17}$  cm (Sikora et al. 2005). There have also been explicit inferences of component acceleration based on radio proper motion and X-ray emission measurements for the jets in the quasars 3C 345 (Unwin et al. 1997) and 3C 279 (Piner et al. 2003). Extended acceleration in the 3C 345 jet has been independently indicated by the higher apparent speeds of jet components located further away from the nucleus (Lobanov & Roland 2005) and by the observed luminosity variations of the moving components (Lobanov & Zensus 1999). Similar effects in other blazars (e.g. Homan et al. 2001) suggest that parsec-scale acceleration to relativistic speeds may be a common feature of AGN jets. Vlahakis & Königl (2004) argued that these observations are most naturally interpreted in terms of magnetic driving and employed self-similar relativistic jet solutions to generate model fits to the 3C 345 data in support of this conclusion.

While the semi-analytic solutions have been useful in indicating basic properties of the magnetic acceleration process and in providing valuable clues to the interpretation of the observational data, more general solutions are needed to confirm these results and to gain a fuller understanding of the generation of relativistic jets in AGNs. In particular, numerical simulations are needed to find out whether the self-similar model captures the essential properties of outflows that obey realistic boundary conditions and that are not required to be in a steady state. Among the questions that such simulations could answer are: (1) Do disk outflows in fact approach a steady state, and, if they do, is that state stable? (2) Is the acceleration indeed generally extended, and to what extent does the asymptotic state of the self-similar solutions approximate the far-field behaviour of more realistic outflows? (3) Do any new traits emerge when the restrictions imposed by the self-similarity assumption are removed? Of particular interest is the question of the ability of the magnetic driving mechanism to accelerate outflows to high Lorentz factors with high efficiency over astrophysically relevant distance scales. Another important question is whether highly relativistic flows can be strongly collimated by purely magnetic stresses. There have been lingering doubts over these issues in the literature (see Sec-

tion 5.1), and although they have already received tentative answers, a full numerical study could help to settle them once and for all.

Although there have already been several reported simulations of the formation of jets in black-hole accretion flows using relativistic (in fact, *general*-relativistic) MHD codes, so far they have provided only partial answers to the above questions. The existing calculations indicate that magnetic acceleration indeed operates over several decades in radius and can accelerate jets to relativistic speeds. However, the extended nature of the acceleration typically results in the bulk Lorentz factor reaching only a small fraction of its potential asymptotic value by the time the simulation is terminated. For example, in the longest jet simulated to date, which extended to  $\sim 10^4$  times the gravitational radius  $r_g$  of the central black hole (McKinney 2006), the Lorentz factor on the largest computed scale was  $\sim 10$ , which is just  $\sim 10^{-2} - 10^{-3}$  of the estimated asymptotic value. This impressive simulation deals with an extremely complex system of which the jet is only one component, the other being the black hole, the accretion disk, the disk corona, the low-speed “wall jet,” and their surroundings. Ultimately, this is the kind of simulation one wants to carry out in order to fully understand the dynamics of AGN outflows. However, they are also very challenging from the computational point of view. One major concern is that, in view of the extended nature of its acceleration, the jet is particularly vulnerable to numerical diffusion and dissipation. These numerical effects may partly explain why the quantity  $\Gamma_\infty$  in the above-cited paper, which is the same as our  $\mu$  (equation 15) and should be a field-line constant, in fact decreases by about one order of magnitude along a mid-level field line in the simulated jet (see Fig. 7 in McKinney 2006).

In this paper we address the above questions through numerical simulations specifically designed for investigating the key aspects of ideal-MHD acceleration of relativistic jets. In the first place, we use a numerical scheme based on a linear Riemann solver (Komissarov 1999) that does not need a large artificial diffusion for numerical stability. This distinguishes it from most other schemes for relativistic MHD, including those that are based on HLL, KT and similar flux prescriptions (e.g. Gammie et al. 2003; Duez et al. 2005; Koide et al. 1999; Anninos et al. 2006; Shibata & Sekuguchi 2005; Anderson et al. 2006a; Del Zanna et al. 2003; Antón et al. 2006). Simple one-dimensional tests suggest that this should lead to a noticeably greater accuracy in two-dimensional problems that involve stationary flows that are aligned with the computational grid (Komissarov 2006). Secondly, instead of studying jet propagation through some ambient medium, we consider the case of a flow in a funnel with solid walls. This allows us to avoid the errors that would otherwise be caused by numerical mass diffusion and dissipation at the interface. Finally, we employ elliptical (or spherical) coordinates adapted to the chosen paraboloidal (or conical) shape of the funnel. This allows us to have the jet well resolved everywhere (using a fixed number of grid points across the funnel) and to benefit from the close alignment of the flow with the computational grid. These careful measures in conjunction with a grid-extension method enable us, for the first time, to track the acceleration and collimation processes to their completion.

We describe the basic equations in Section 2 and the numerical calculations in Section 3. The simulation results are presented in Section 4 and discussed in Section 5. We summarize in Section 6.

## 2 BASIC EQUATIONS

Since most of the acceleration takes place far away from the source, we assume that the space-time is flat. Moreover, the flow is described in an inertial frame at rest relative to the source. In this case we can write the system of ideal relativistic MHD as follows. The *continuity equation*

$$(1/c)\partial_t(\sqrt{-g}\rho u^t) + \partial_i(\sqrt{-g}\rho u^i) = 0, \quad (1)$$

where  $\rho$  is the rest mass density of matter,  $u^\nu$  is its 4-velocity, and  $g$  is the determinant of the metric tensor; the *energy-momentum equations*

$$(1/c)\partial_t(\sqrt{-g}T^\nu_t) + \partial_i(\sqrt{-g}T^\nu_i) = \frac{\sqrt{-g}}{2}\partial_\nu(g_{\alpha\beta})T^{\alpha\beta}, \quad (2)$$

where  $T^{\kappa\nu}$  is the total stress-energy-momentum tensor; the *induction equation*

$$(1/c)\partial_t(B^i) + e^{ijk}\partial_j(E_k) = 0, \quad (3)$$

where  $e_{ijk} = \sqrt{\gamma}\epsilon_{ijk}$  is the Levi-Civita tensor of the absolute space ( $\epsilon_{123} = 1$  for right-handed systems and  $\epsilon_{123} = -1$  for left-handed ones) and  $\gamma$  is the determinant of the spatial part of the metric tensor ( $\gamma_{ij} = g_{ij}$ ); the *solenoidal condition*

$$\partial_i(\sqrt{\gamma}B^i) = 0. \quad (4)$$

The total stress-energy-momentum tensor,  $T^{\kappa\nu}$ , is a sum of the stress-energy momentum tensor of matter

$$T_{(m)}^{\kappa\nu} = wu^\kappa u^\nu / c^2 + pg^{\kappa\nu}, \quad (5)$$

where  $p$  is the thermodynamic pressure and  $w$  is the enthalpy per unit volume, and the stress-energy momentum tensor of the electromagnetic field

$$T_{(e)}^{\kappa\nu} = \frac{1}{4\pi} \left[ F^{\kappa\alpha} F^\nu_\alpha - \frac{1}{4}(F^{\alpha\beta} F_{\alpha\beta})g^{\kappa\nu} \right], \quad (6)$$

where  $F^{\nu\kappa}$  is the Maxwell tensor of the electromagnetic field. The electric and magnetic field are defined as measured by an observer stationary relative to the spatial grid, which gives

$$B^i = \frac{1}{2}e^{ijk}F_{jk} \quad (7)$$

and

$$E_i = F_{it}. \quad (8)$$

In the limit of ideal MHD

$$E_i = -e_{ijk}v^j B^k / c, \quad (9)$$

where  $v^i = u^i / u^t$  is the usual 3-velocity of the plasma.

We use an isentropic equation of state

$$p = Q\rho^s, \quad (10)$$

where  $Q = \text{const}$  and  $s = 4/3$ . Since we are interested in the magnetic acceleration of cold flows, we make  $Q$  very small, so the gas pressure is never a dynamical factor. This relation enables us to exclude the energy equation from the integrated system. However, the momentum equation remains

intact, including the nonlinear advection term. Therefore, if the conditions for shock formation were to arise, our calculation would capture that shock.<sup>3</sup>

### 2.1 Field-line constants

The poloidal magnetic field is fully described by the azimuthal component of the vector potential,

$$B^i = \frac{1}{\sqrt{\gamma}}\epsilon^{ij\phi}\frac{\partial A_\phi}{\partial x^j}. \quad (11)$$

For axisymmetric solutions  $A_\phi = \Psi/2\pi$ , where  $\Psi(x^i)$ , the so-called magnetic flux function, is the total magnetic flux enclosed by the circle  $x^i = \text{const}$  ( $x^i$  being the coordinates of the meridional plane). Stationary and axisymmetric ideal MHD flows have 5 quantities that propagate unchanged along the magnetic field lines and thus are functions of  $\Psi$  alone. These are  $k$ , the rest-mass energy flux per unit magnetic flux;  $\Omega$ , the angular velocity of magnetic field lines;  $l$ , the the total angular momentum flux per unit rest-mass energy flux;  $\mu$ , the total energy flux per unit rest-mass energy flux; and  $Q$ , the entropy per particle. For cold flows ( $Q = 0$ ,  $w = \rho c^2$ ) we have

$$k = \frac{\rho u_p}{B_p}, \quad (12)$$

$$\Omega = \frac{v^\phi}{r} - \frac{v_p}{r} \frac{B^\phi}{B_p}, \quad (13)$$

$$l = -\frac{I}{2\pi kc} + r u^\phi, \quad (14)$$

and

$$\mu = \Gamma(1 + \sigma), \quad (15)$$

where  $u_p = \Gamma v_p$  is the magnitude of the poloidal component of the 4-velocity,  $B_p$  is the magnitude of the poloidal component of the magnetic field,  $r$  is the cylindrical radius,

$$I = \frac{c}{2}rB^\phi \quad (16)$$

is the total electric current flowing through a loop of radius  $r$ ,  $\sigma$  is the ratio of the Poynting flux to the matter (kinetic plus rest-mass) energy flux, and

$$\Gamma\sigma = -\frac{\Omega I}{2\pi kc^3} \quad (17)$$

is the Poynting flux per unit rest-mass energy flux. (Here and in the rest of the paper we use a hat symbol over vector indices to indicate their components in a normalized coordinate basis.) From equation (15) it follows that the Lorentz factor  $\Gamma$  cannot exceed  $\mu$ .

## 3 NUMERICAL SIMULATIONS

To maintain a firm control over the jet's confinement and to prevent complications related to numerical diffusion of

<sup>3</sup> Since entropy is fixed the compression of our shocks would be the same as for continuous compression waves. This gives a higher jump in density for the same jump in pressure than in a proper dissipative shock. Fortunately, we do not need to contend with this issue in practice as shocks do not form in our simulations.

the dense nonrelativistic plasma from the jet's surroundings, we study outflows that propagate inside a solid funnel of a prescribed shape.<sup>4</sup> Specifically, we consider axisymmetric paraboloidal funnels

$$z \propto r^a,$$

where  $z$  and  $r$  are the cylindrical coordinates of the funnel wall. This suggests the utilization of a system of coordinates in which the funnel wall is a coordinate surface. For a conical jet ( $a = 1$ ) we use spherical coordinates, whereas for jets with  $a > 1$  we employ elliptical coordinates  $\{\xi, \eta, \phi\}$ , where

$$\xi = rz^{-1/a} \quad (18)$$

and

$$\eta^2 = \frac{r^2}{a} + z^2 \quad (19)$$

(see Appendix A for details).<sup>5</sup>

We use a Godunov-type numerical code based on the scheme described in Komissarov (1999). To reduce numerical diffusion we applied parabolic reconstruction instead of the linear one of the original code. Our procedure, in brief, was to calculate minmod-averaged first and second derivatives and use the first three terms of the Taylor expansion for spatial reconstruction. This simple procedure has resulted in a noticeable improvement in the solution accuracy even though the new scheme is still not 3rd-order accurate because of the non-uniformity of the grid.

The grid is uniform in the  $\xi$  direction (the polar angle direction when we use spherical coordinates), where in most runs it has a total of 60 cells. To check the convergence, some runs were repeated with a doubled resolution. The cells are elongated in the  $\eta$  direction (the radial direction when we use spherical coordinates), reflecting the elongation of the funnel. For very elongated cells we observed numerical instability, so we imposed an upper limit of 40 on the length/width ratio.

To speed up the simulations, we implemented a sectioning of the computational grid as described in Komissarov & Lyubarsky (2004). In each section, which is shaped as a ring, the numerical solution is advanced using a time step based on the local Courant condition. It is twice as large as the time step of the adjacent inner ring and twice as small as the time step of the adjacent outer ring. This approach is particularly effective for conical flows but less so for highly collimated, almost cylindrical configurations.

<sup>4</sup> In real astrophysical systems, the shape of the boundary is determined by the spatial distribution of the pressure or the density of the confining ambient medium (e.g. Blandford & Rees 1974; Königl 1982; Komissarov 1994). The effective ambient pressure distributions implied by the adopted funnel shapes are considered in Section 5.2.

<sup>5</sup> The equations are dimensionalized in the following manner. The unit of length,  $L$ , is such that  $\eta_i = 1L$ , where the subscript  $i$  refers to the inlet boundary. The unit of time is  $T = L/c$ . The unit of mass is  $M = L^3 B_0^2 / 4\pi c^2$ , where  $B_0$  is the dimensional magnitude of the  $\eta$  component of magnetic field at the inlet (so the dimensionless magnitude of  $B^{\hat{\eta}}$  at the inlet is  $\sqrt{4\pi}$ ). In applications,  $L$  is the length scale of the launch region (e.g. the radius of the event horizon if the jet originates in a black hole),  $T$  is the light crossing time of that region and  $B_0$  is the typical strength of the poloidal magnetic field at the origin.

### 3.1 Boundary conditions

#### 3.1.1 Inlet boundary

We treat the inlet boundary,  $\eta_i = 1$ , as a surface of a perfectly conducting rotator and consider two rotation laws,

$$\Omega = \Omega_0 \quad (20)$$

and

$$\Omega = \Omega_0 [1 - 3(\xi/\xi_j)^2 + 2(\xi/\xi_j)^3], \quad (21)$$

where  $\xi_j$  marks the jet boundary. The angular velocity profile is directly related to the distribution of the return electric current in the jet (see equation 28 below). In fact, the current is driven by the electric field associated with the rotating poloidal field, and charge conservation requires the circuit to eventually close. In the case of constant  $\Omega$  the return current flows over the jet boundary. For the rotation law (21) it is distributed over the jet body as a volume current, the current changing sign at  $\xi \simeq \xi_j/2$ . Thus, we cover the two generic types of electric current distribution. The solid-body rotation law provides a very good description of the behaviour of magnetic field lines that thread the horizon of a black hole. This choice is therefore entirely appropriate for the black-hole theory of relativistic AGN jets. The differential rotation law is more suitable to the accretion-disk theory, although it admittedly does not correspond to a realistic velocity field (which is hard to model given the limitations of our numerical technique).

The condition of perfect conductivity allows us to fix the azimuthal component of the electric field and the  $\eta$  component of the magnetic field:

$$E_\phi = 0, \quad B^{\hat{\eta}} = B_0 \quad \text{at} \quad \eta = \eta_i. \quad (22)$$

From the first of these conditions we derive

$$v^{\hat{\xi}} = \frac{v^{\hat{\eta}}}{B^{\hat{\eta}}} B^{\hat{\xi}} \quad (23)$$

and (using equation 13)

$$v^{\hat{\phi}} = r\Omega + \frac{v^{\hat{\eta}}}{B^{\hat{\eta}}} B^{\hat{\phi}}. \quad (24)$$

We have also experimented with non-uniform distributions of the magnetic field, in particular with  $B^{\hat{\eta}}$  decreasing with  $\xi$ . The results were not significantly different as the field distribution downstream of the inlet underwent a rapid rearrangement that restored the transverse force balance.

On the assumption of a cold (i.e. zero thermal energy) jet, the flow at the inlet boundary is necessarily super-slow-magnetosonic. This means that both the density and the radial component of the velocity can be prescribed some fixed values:

$$\rho = \rho_0, \quad v^{\hat{\eta}} = v_{p0}.$$

In the simulations we used  $v_{p0} = 0.5c$ , which was a choice of convenience. On the one hand, this value is sufficiently small to insure that the flow at  $\eta = 1$  is sub-Alfvénic and hence that the Alfvén and fast-magnetosonic critical surfaces are located downstream of the inlet boundary. On the other hand, it is large enough to promote a rapid settlement to a steady state (keeping in mind that the speed of a steady-state flow remains constant along the symmetry axis). Because of the sub-Alfvénic nature of the inlet flow,

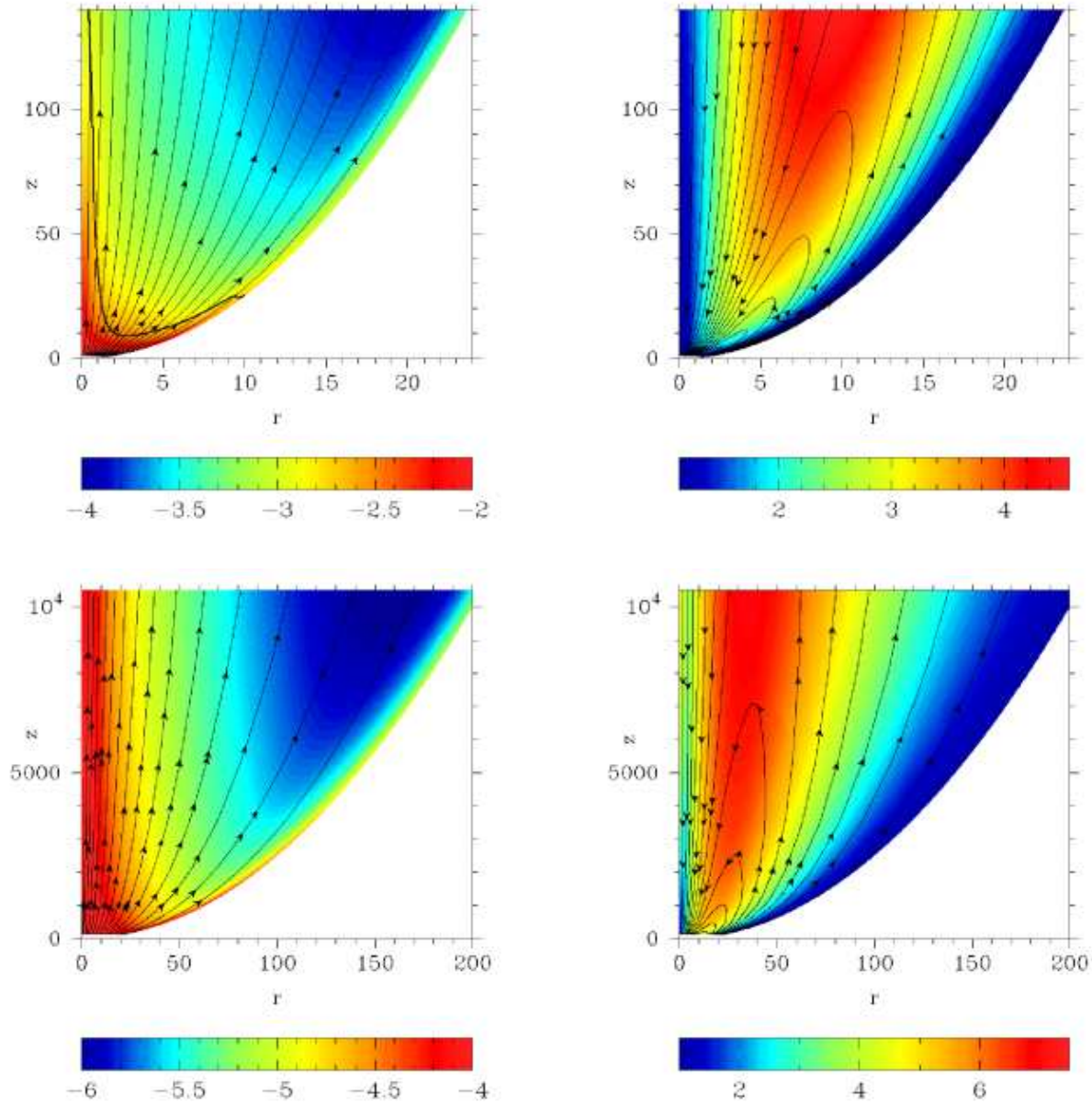


**Figure 1.** Model C1. Left panels show  $\log_{10} \Gamma\rho$  (colour), where  $\Gamma\rho$  is the jet density as measured in the laboratory frame, and magnetic field lines. Right panels show the Lorentz factor (colour) and the current lines. The thick solid line in the top-left panel denotes the surface where the flow becomes superfast in the  $\eta$  direction. The top panels show the solution for the first grid sector, whereas the bottom panels show the combined solution for the second and third grid sectors.

we cannot fix the other components of the magnetic field and the velocity – they are to be found as part of the global solution. Following the standard approach we extrapolate  $B^{\hat{\phi}}$  and  $B^{\hat{\xi}}$  from the domain into the inlet boundary cells. We then compute  $v^{\hat{\phi}}$  and  $v^{\hat{\xi}}$  from equations (23) and (24).

In the case of differential rotation the magnitude of the angular velocity is chosen in such a way that the Alfvén surface of the jet is near the jet origin, its closest point being located at a distance of  $\sim 1.5$  times the initial jet radius from the inlet surface. In the case of solid-body rotation the Alfvén surface almost coincides with the light cylinder,

whose radius  $r_{lc} \equiv c/\Omega$  is only 50% larger than the initial jet radius.

The inlet density is chosen so that all jets have very similar values of  $\mu$  and  $\sigma$ . In particular, for the models with uniform  $\Omega$  we have  $\mu_{\max} \simeq 18$ , and for the models with non-uniform  $\Omega$  we have  $\mu_{\max} \simeq 12$ .

### 3.1.2 Other boundaries

The computational domain is always chosen to be long enough for the jet to be super-fast-magnetosonic when it approaches the outlet boundary  $\eta = \eta_o$ . This justifies the

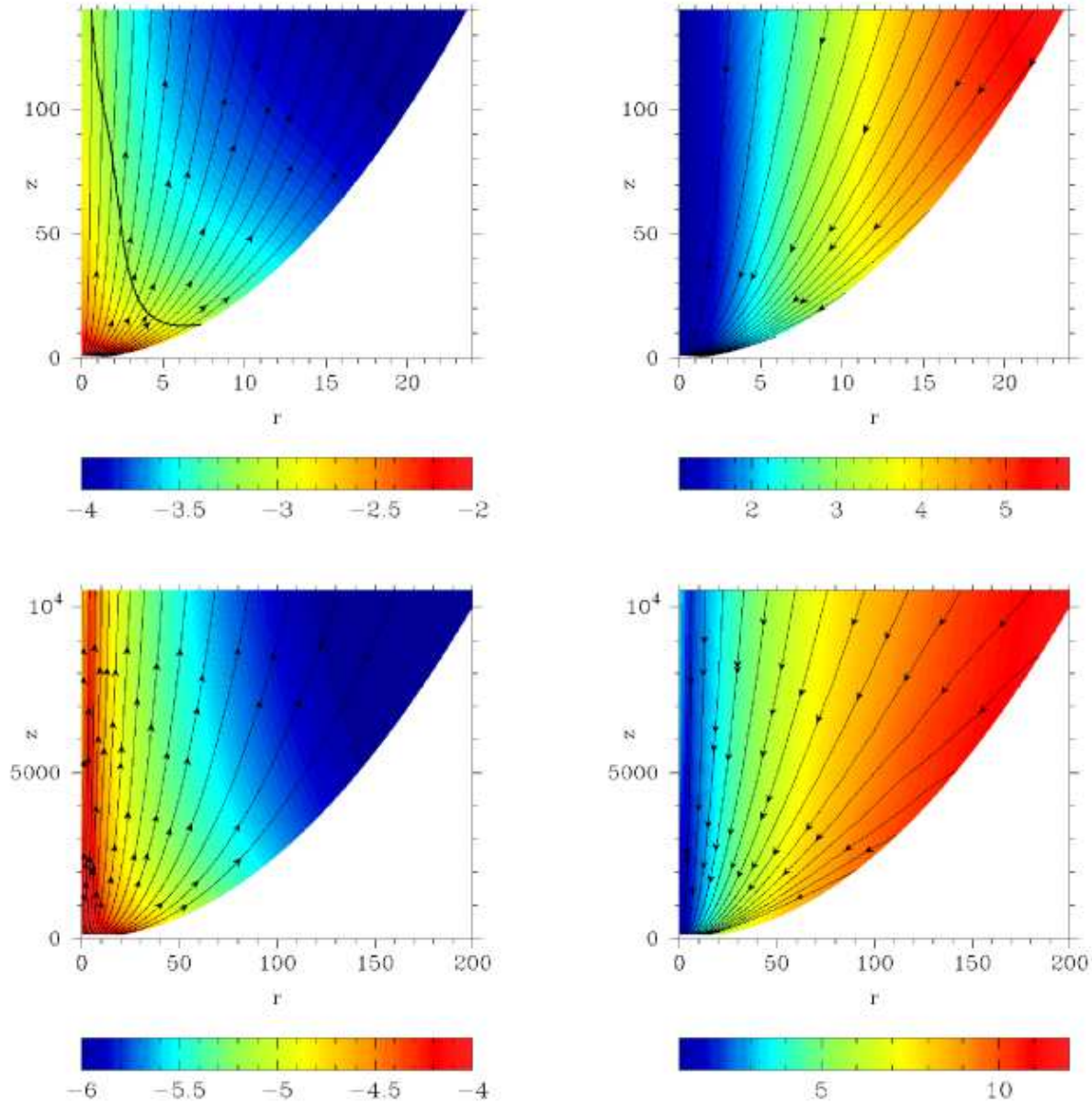


**Figure 2.** Same as Fig. 1, but for Model C2.

use of radiative boundary conditions at this boundary (i.e. we determine the state variables of the boundary cells via extrapolation of the domain solution).

At the polar axis,  $\xi = 0$ , we impose symmetry boundary conditions for the dependent variables that are expected to pass through zero there,

$$f(-\xi) = -f(\xi).$$

These variables include  $B^{\hat{\xi}}$ ,  $B^{\hat{\phi}}$ ,  $u^{\hat{\xi}}$  and  $u^{\hat{\phi}}$ . For other variables we impose a “zero second derivative” condition,

$$\partial^2 f / \partial \xi^2 = 0,$$

which means that we use linear interpolation to calculate the values of these variables in the boundary cells.

We do this in order to improve the numerical represen-

tation of a narrow core that develops in all cases as a result of the magnetic hoop stress. Within this core the gradients in the  $\xi$  direction are very large and the usual zero-gradient condition,  $f(-\xi) = f(\xi)$ , results in increased numerical diffusion in this region. We have checked that this has a noticeable effect only on the axial region and that the global solution does not depend on which of these two conditions is used.

At the wall boundary,  $\xi = \xi_j$ , we use a reflection condition,

$$f(\xi_j + \Delta\xi) = -f(\xi_j - \Delta\xi),$$

for  $B^{\hat{\xi}}$  and  $u^{\hat{\xi}}$  and a zero-gradient condition for all other variables.

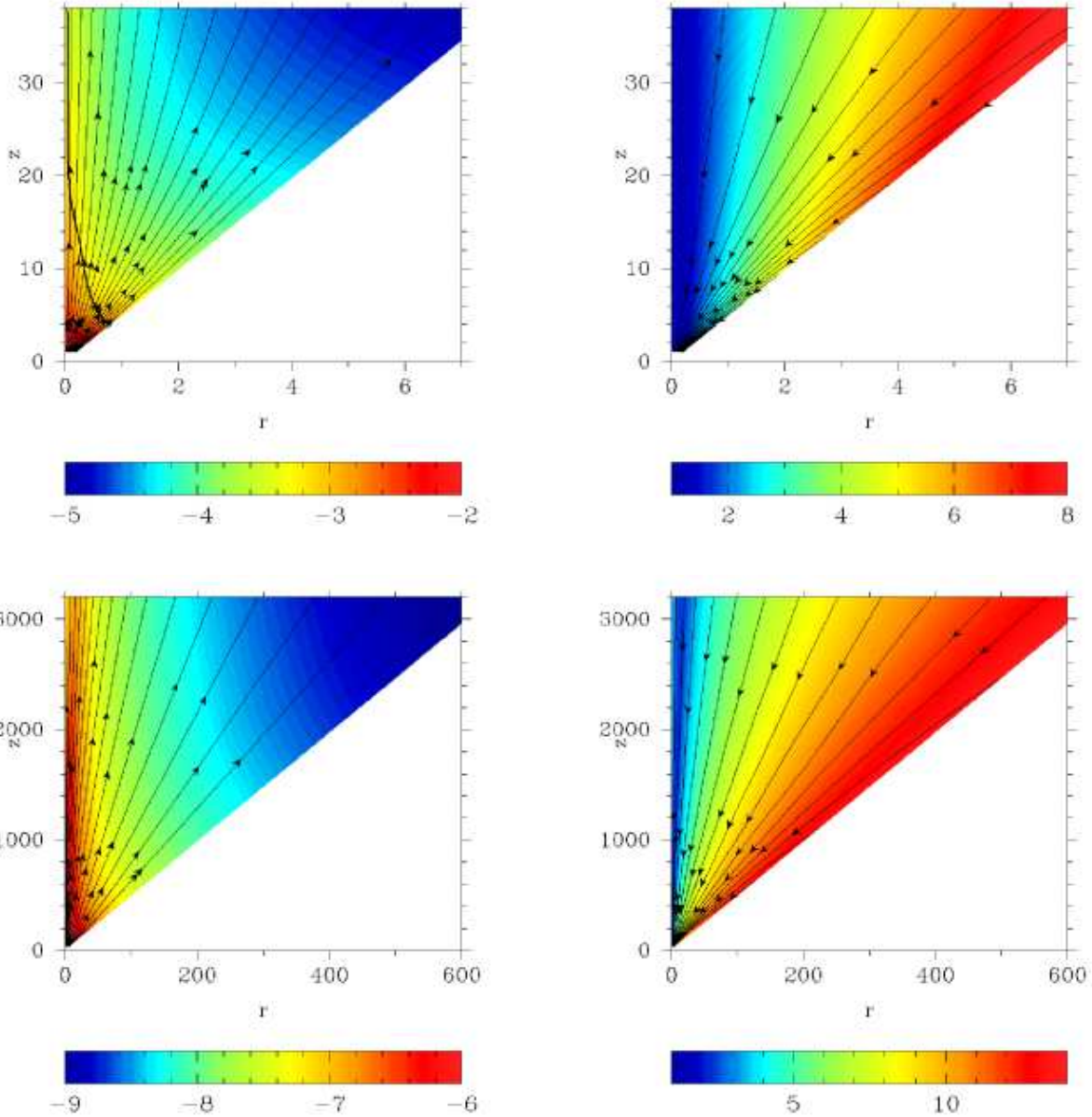


**Figure 3.** Same as Fig. 1, but for Model A2.

### 3.2 Initial setup

The initial configuration corresponds to a non-rotating, purely poloidal magnetic field with approximately constant magnetic pressure across the funnel. The plasma density within the funnel is set to a small value so that the outflow generated at the inlet boundary can easily sweep it away. In order to speed this process up the  $\eta$  component of velocity inside the funnel is set equal to  $0.7c$ , whereas the  $\xi$  component is set equal to zero.

### 3.3 Grid extensions

The inner rings of the grid, where the grid cells are small and so is the time step, are the computationally most inten-

sive regions of the simulation domain. If we kept computing these inner rings during the whole run then we would not be able to advance very far from the jet origin. Fortunately, the trans-sonic nature of the jet flow allows us to cease computations in the inner region once the solution there settles to a steady state. To be more precise, we cut the funnel along the  $\xi$ -coordinate surfaces into overlapping sectors with the intention of computing only within one sector at any given time, starting with the sector closest to the inlet boundary. Once the solution in the “active” sector settles to a steady state we switch to the subsequent sector, located further away from the inlet. During the switch the solution in the outermost cells of the active sector is copied into the corresponding inner boundary cells of the subsequent sector. During the computation within the latter sector these in-



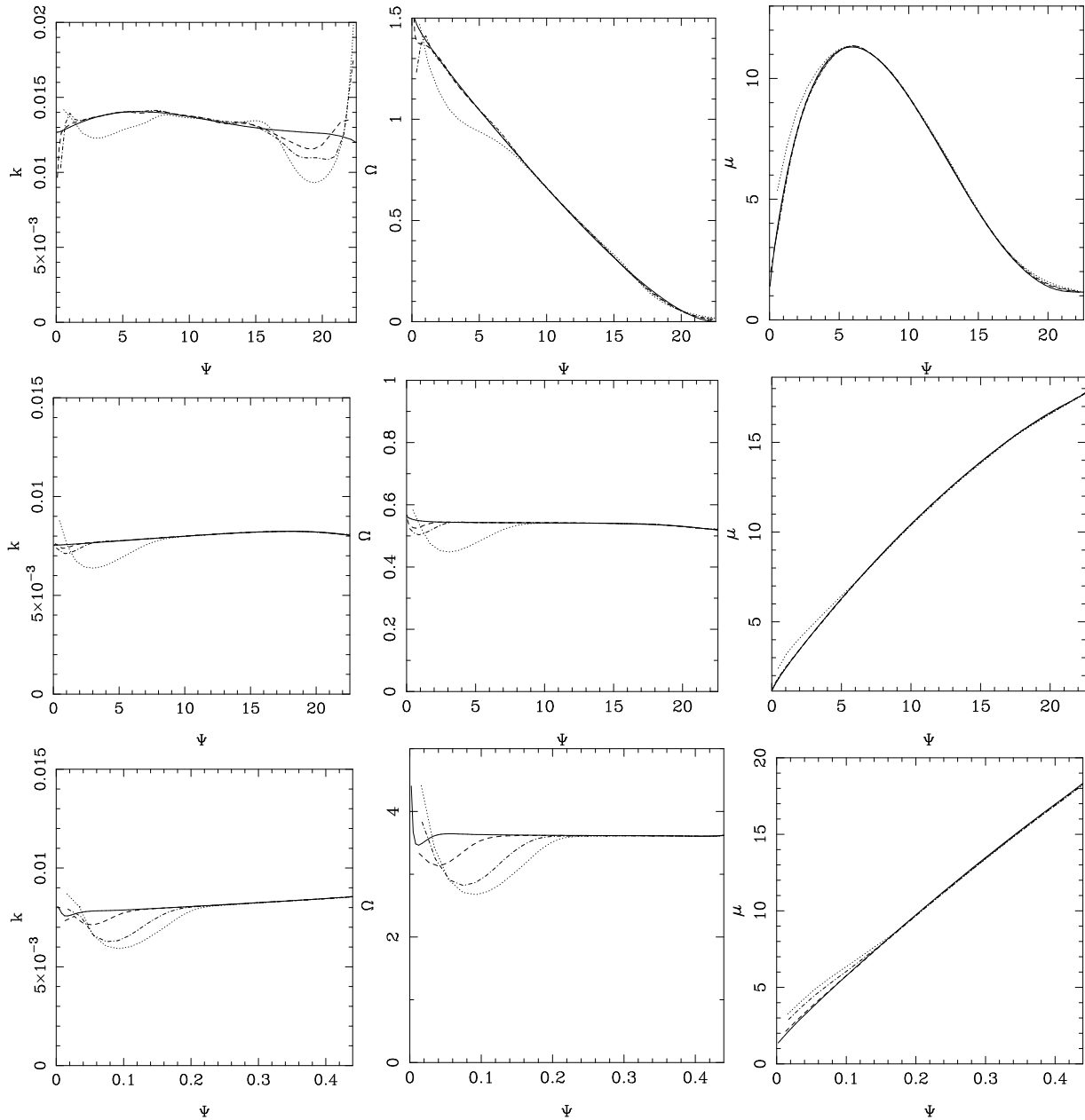


**Figure 4.** Flow constants  $k(\Psi)$ ,  $\Omega(\Psi)$  and  $\mu(\Psi)$  at different distances from the source for models C1 (top row), C2 (middle row) and A2 (bottom row). In all cases the solid lines show the constants at the injection surface ( $\eta = 1$ ). The deviations from these values further downstream are due to a gradual accumulation of numerical errors. For models C1 and C2 the dashed line corresponds to  $\eta = 10^2$ , the dash-dotted line to  $\eta = 10^3$ , and the dotted line to  $\eta = 10^4$ . For model A2 the dashed line corresponds to  $\eta = 2 \times 10^2$ , the dash-dotted line to  $\eta = 2 \times 10^3$ , and the dotted line to  $\eta = 2 \times 10^4$ .

ner boundary cells are not updated. Surely, this procedure is justified only when the flow in a given sector cannot communicate with the flow in the preceding sector through hyperbolic waves, and thus we need to ensure that the Mach cone of the fast-magnetosonic waves points outward at the sector interfaces. This condition can be written as

$$\begin{aligned}
 (\Gamma v^{\hat{\eta}})^4 - (\Gamma v^{\hat{\eta}})^2 \left( \frac{b^2}{4\pi w/c^2} + \frac{c_s^2}{1 - c_s^2/c^2} \right) + \\
 + \frac{c_s^2}{1 - c_s^2/c^2} \frac{(B^{\hat{\eta}})^2}{4\pi w/c^2} \left( 1 - \frac{r^2}{r_{lc}^2} \right) > 0, \quad (25)
 \end{aligned}$$

where  $c_s^2 = spc^2/w$  (see equation 10) and  $b = (B^2 - E^2)^{1/2}$  is the magnetic field magnitude in the fluid frame (see Appendix B for details). In the cold limit this reduces to

$$v^{\hat{\eta}} > \left[ 1 - \left( v^{\hat{\epsilon}}/c \right)^2 - \left( v^{\hat{\phi}}/c \right)^2 \right]^{1/2} c_f, \quad (26)$$

where  $c_f = b/(4\pi\rho + b^2/c^2)^{1/2}$  is the isotropic fast speed in the fluid frame. Thus, the jet has to be super-fast in the  $\eta$  direction at the sector interfaces. In Figs. 1–3 the location of the surface where  $v^{\hat{\eta}} = c_f$  is shown by a thick solid line: to the right of this line  $v^{\hat{\eta}} > c_f$ . One can see that the transition

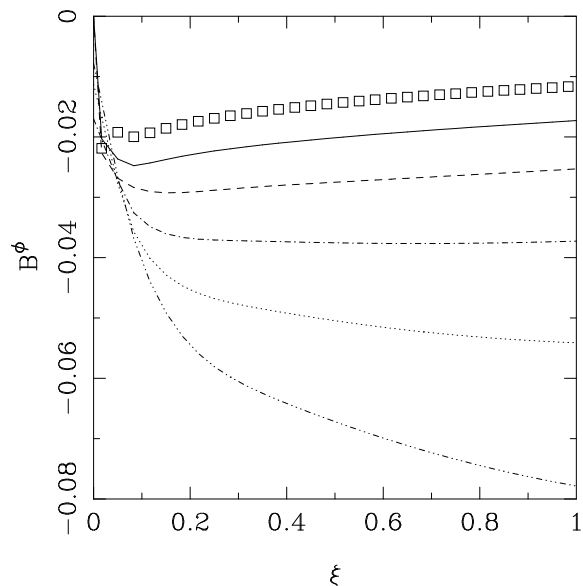


**Figure 5.** Development of the line current in model C2. The figure shows the azimuthal magnetic field at  $\eta = 200, 400, 800, 1600, 3200$  and  $6400$  (from bottom to top). The solution at  $\eta = 6400$  is plotted as squares.

to the super-fast regime occurs well inside the first sector. (Note that when  $v^{\tilde{\eta}} > c_f$  the inequality 26 is satisfied.)

In these simulations we normally used 4 or 5 sectors, with each additional sector being ten times longer than the preceding one. This technique has enabled us to reduce the computational time by up to three orders of magnitude, depending on the funnel geometry. Although the grid extension can in principle be continued indefinitely, there are other factors that limit how far along the jet one can advance in practice. Firstly, once the paraboloidal jets become highly collimated the required number of grid cells along the jet axis increases, and each successive sector becomes more expensive than the previous one. Secondly, computational errors due to numerical diffusion gradually accumulate in the downstream region of the flow and the solution becomes progressively less accurate (see Fig. 4).

## 4 RESULTS

Models A, B, C and D have geometrical power indices  $a = 1, 3/2, 2$  and  $3$ , respectively. Further classification is based on the rotation law: models A1–D1 have non-uniform rotation, whereas models A2–D2 have uniform rotation.

Models with different power indices but the same rotation law show remarkably similar properties. Thus, it is sufficient to show only one of them in greater detail. For this purpose we selected models C1, C2 and A2.

Fig. 1 shows the distribution of the Lorentz factor, the lab-frame rest-mass density, the poloidal magnetic field, and the poloidal electric current for model C1. The top panel presents the solution in the innermost grid sector whereas the bottom panels show the solution in the second and third sectors “glued” together. The density distribution as well as the magnetic field lines clearly indicate that the jet develops a core where the magnetic surfaces become almost

cylindrical.<sup>6</sup> The core is produced by the hoop stress of the toroidal magnetic field that is wound up in the main body of the jet due by the rotation at its base. The ratio of the core radius to the jet radius decreases monotonically with increasing distance from the source until the core eventually becomes unresolved on the grid. The solution then develops what looks like an axial line current. (Such behaviour is also observed in models A2–D2; see Fig. 11).

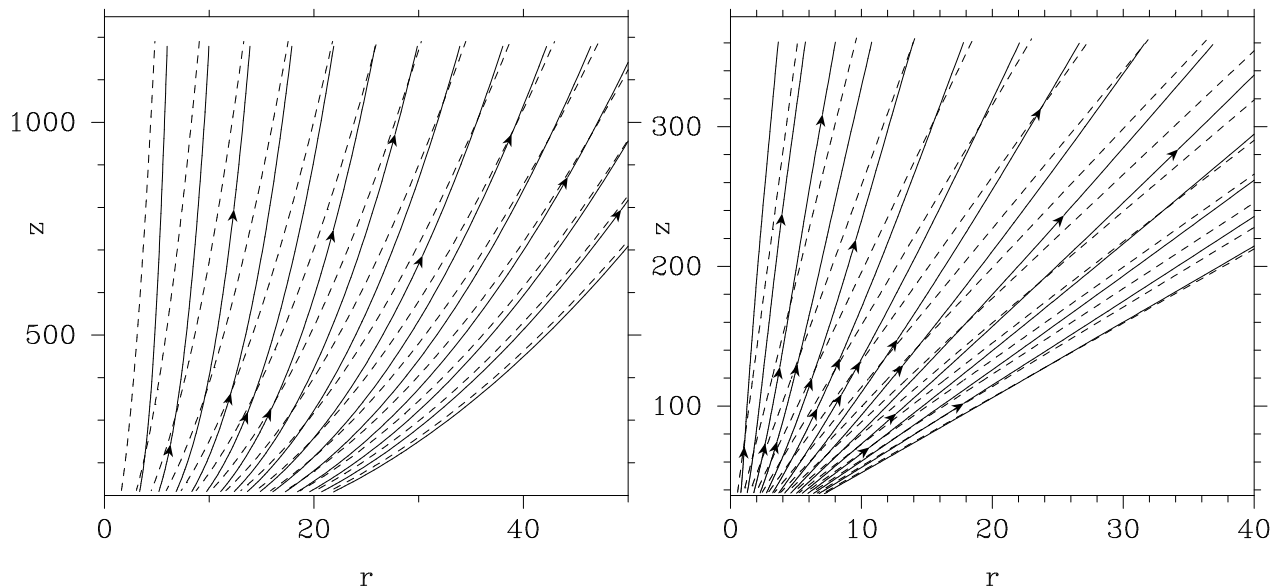
Near the jet boundary, where the angular velocity of the magnetic field lines in model C1 vanishes, the azimuthal magnetic field component is weak and the equilibrium is supported in part by the poloidal field. If the flow were self-similar, one would have  $B_p \propto r_j^{-2}$ ,  $B^\phi \propto r_j^{-1}$ , and the pressure of the azimuthal field in the main body of the jet would eventually become much larger than the pressure of the poloidal field in the boundary sheath, leading to a loss of force balance. In reality, the flow adjusts through a progressive compression of the sheath. Consequently a thin layer of surface current gradually develops as the distance from the source increases. This is why some current lines in the bottom-right panel of Fig. 1 appear to terminate at the jet surface.

The most effective acceleration of the C1 jet occurs at intermediate cylindrical radii, where the angular velocity of the field lines reaches a maximum and the poloidal electric current flows across the jet (so the  $(1/c)\mathbf{j}_p \times \mathbf{B}_\phi$  force is maximized). Note that this aspect of the jet behaviour could not have been studied with the help of self-similar models, in which the current lines do not change direction within the jet. At comparatively small distances from the inlet boundary the maximum acceleration occurs at  $r_{\max} \simeq 0.5 r_j$ , but further downstream  $r_{\max} \simeq 0.25 r_j$ . This is explained by a more effective collimation in the inner region of the jet than at the jet boundary (see discussion following equation 29 in Section 5.1).

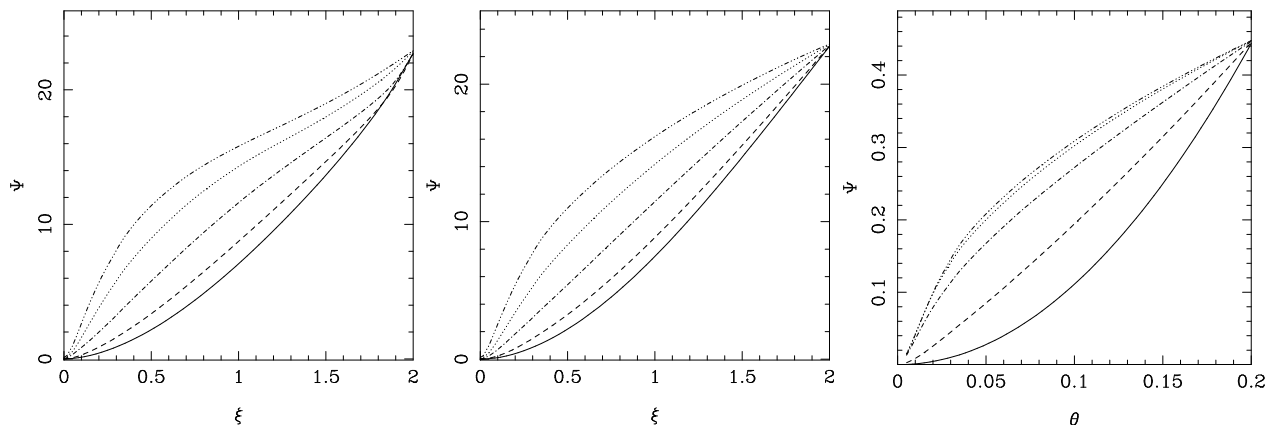
A careful inspection of the velocity field in the lower-right panel of Fig. 1 reveals an additional region of effective acceleration near the jet axis for  $z \geq 10^3$ . This acceleration, however, is unphysical as it is caused by numerical diffusion/dissipation in the core that result from large gradients of the flow variables that develop there. The gradual growth of errors in this region is clearly seen in Fig. 4, which shows the flow constants as functions of  $\Psi$  at various distances from the source. Beyond  $z = 10^4$  the errors become unacceptably large and this makes further continuation of the solution via grid extension meaningless. We note in this connection that, even in the absence of exact analytic solutions, the existence of flow constants makes the jet problem a very useful one for testing RMHD codes and assessing their performance.

Fig. 2 shows the distribution of the Lorentz factor, the lab-frame rest-mass density, the poloidal magnetic field and the poloidal electric current for model C2. One can see that a core still develops but that a boundary sheath is no longer present. This is because the uniform rotation of the magnetic field lines in this model ensures an effective generation of azimuthal magnetic field all the way up to the jet boundary.

<sup>6</sup> The isodensity contours are, in fact, more strongly collimated than the magnetic field lines (or flow streamlines), a trait already identified previously in nonrelativistic (Shu et al. 1995) and moderately relativistic (Li 1996) MHD disk outflows.



**Figure 6.** Poloidal magnetic field lines (solid) and  $\xi = \text{const}$  coordinate lines (dashed) for models C2 (left panel) and A2 (right panel). In all models the magnetic field lines show faster collimation than the coordinate lines.



**Figure 7.** Evolution of the magnetic flux distribution across the jet with distance from the inlet. *Left panel:* model C1. *Middle panel:* model C2. In both cases the solid line corresponds to  $\eta = 10$ , the dashed line to  $\eta = 10^2$ , the dash-dotted line to  $\eta = 10^3$ , the dotted line to  $\eta = 10^4$  and the dash-triply-dotted line to  $\eta = 10^5$ . *Right panel:* model A2. The solid line corresponds to  $\eta = 1$ , the dashed line to  $\eta = 30$ , the dash-dotted line to  $\eta = 3 \times 10^2$ , the dotted line to  $\eta = 3 \times 10^3$  and the dash-triply-dotted line to  $\eta = 3 \times 10^4$ . Note that in the conical case we use the spherical coordinate  $\theta = \arctan \xi$  (in radians) rather than the  $\xi$  coordinate.

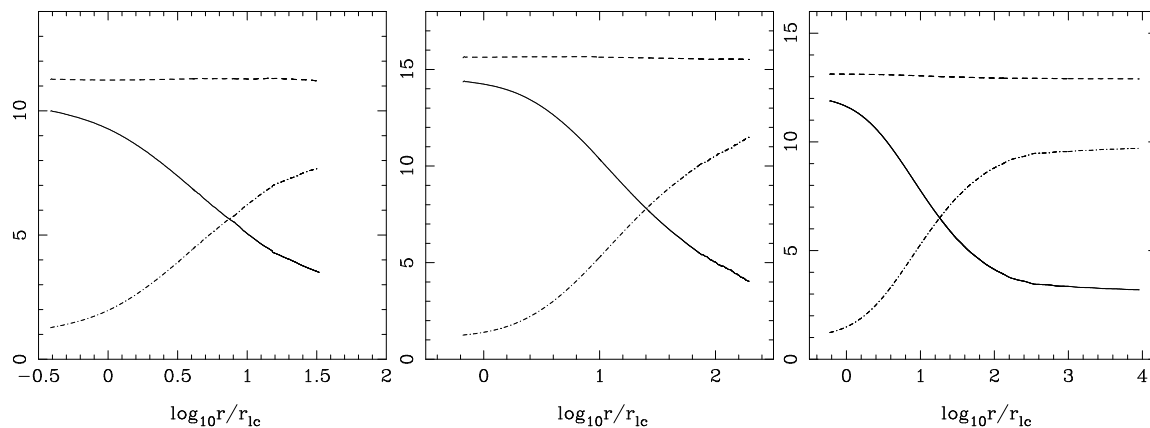


**Figure 8.**  $\Gamma\sigma$  (solid line),  $\mu$  (dashed line) and  $\Gamma$  (dash-dotted line) along a magnetic field line as a function of cylindrical radius for models C1 (left panel), C2 (middle panel) and A2 (right panel).

Fig. 5 shows the development of an axial line current in this solution, a result of the gradual decrease of the core radius relative to the jet radius (similar to what is seen in model C1). Note, however, that the light cylinder is unresolved at the distance where the line current is observed. Thus, what looks like a line current could be a smoothly distributed current inside the light cylinder.

Inside the jet the electric current flows inward everywhere and current closure is achieved via a surface current. The radial component of the current peaks near the boundary, resulting in a higher  $(1/c)\mathbf{j}_p \times \mathbf{B}_\phi$  force and a more effective plasma acceleration in this region.

As in the C1 solution, the numerical errors in model C2 grow most rapidly near the jet axis (see Fig. 4), although they are somewhat smaller in this case. Moreover, the most interesting region of the flow, where the acceleration is most effective, is now far from the axis and does not suffer from these errors as much as in model C1. This feature is characteristic not only of models C but of all the other models as well. For this reason we decided to focus our attention on the models with uniform rotation, A2–D2, and in the rest of this section we present results mainly for these solutions. This choice is further motivated by the fact that models with a non-uniform rotation do not seem to exhibit any significant differences with respect to the uniform-rotation models besides those that we have already described.

Given the results of previous analytical and numerical studies, which suggested poor self-collimation of relativistic magnetized flows (see references in Section 5.1), one could have expected the magnetic flux surfaces to almost mirror the imposed shape of the jet boundary. However, our results indicate that the outflows collimate significantly faster, and that this property is manifested not only by jets with paraboloidal boundaries but also by the ones that are confined by a conical wall (see Fig. 3). Fig. 6 shows the magnetic flux surfaces and the coordinate surfaces  $\xi = \text{const}$  for models A2 and C2. In both cases the magnetic flux surfaces clearly do not diverge as fast as the coordinate surfaces. This effect is further demonstrated by Fig. 7, which shows the evolution of the magnetic flux distribution across these jets (as well as the jet of model C1) with distance from the origin. It is seen that the magnetic flux becomes progressively more concentrated toward the symmetry axis as the flow moves further downstream.

The left and middle panels of Fig. 8 show the evolution of  $\mu$ ,  $\Gamma\sigma$  and  $\Gamma$  along selected magnetic surfaces for models C1 and C2. For model C1 this flux surface is in the middle part of the jet, where the flow accelerates most rapidly; it encloses  $\sim 1/3$  of the total magnetic flux in the jet. For model C2 this surface is near the jet boundary, enclosing  $\sim 5/6$  of the total magnetic flux in the jet. One can see that  $\mu$  remains very nearly constant on the surfaces, indicating that the flow has reached a steady state and that the computational errors that we have described above are fairly small. The Lorentz factor at first grows linearly with cylindrical radius but then enters an extended domain of logarithmic growth. The linear behaviour was previously found in the magnetically dominated regime of self-similar solutions (e.g. Vlahakis & Königl 2003a), whereas the logarithmic behaviour was shown to characterize the acceleration in the asymptotic matter-dominated zone (e.g. Begelman & Li 1994). The range of Lorentz factors in the solutions derived

in this paper is evidently too narrow to allow us to probe the linear growth regime, but we expect that this could be done in our forthcoming paper where we consider higher- $\Gamma_\infty$  flows.

The magnetization function  $\sigma$  eventually becomes less than 1, signaling a transition to the matter-dominated regime. The right panel of Fig. 8 shows the evolution of  $\mu$ ,  $\Gamma\sigma$  and  $\Gamma$  along the magnetic flux surface of model A2 that again encloses  $\sim 5/6$  of the total magnetic flux in the jet. This conical jet also exhibits a very effective initial acceleration and a transition to a matter-dominated regime. In this case the growth of the Lorentz factor saturates when it reaches  $\Gamma \simeq 10$ , a value that corresponds to an acceleration efficiency  $\Gamma/\mu$  of 77%. Although the setup of our conical jet model most closely evokes the conical flow geometries that have in previous works produced very inefficient accelerations (see Section 5.1), the results displayed in Fig. 8 demonstrate that this case is not inherently different from the other ones. We discuss the reasons for this in Section 5.1. It is also worth noting that, while our choice of flux surfaces in Fig. 8 was arbitrary, the behaviour along these surfaces is fairly representative. To demonstrate this we show in Fig. 9 the variation of the same parameters *across* the jets at large distances from the inlet. One can see that the jets are matter-dominated throughout the entire cross-section.

Fig. 10 compares the growth rates of  $\Gamma$  in models A2–D2. The numerical errors in these models are less restrictive than in models A1–D1 and make it possible to extend the simulations to larger spatial scales. Each of the plotted curves corresponds to the magnetic surface near the jet boundary that encloses  $\sim 5/6$  of the total magnetic flux. The left panel shows  $\Gamma$  as a function of the cylindrical radius normalized by the light-cylinder radius. The most interesting feature of this figure is the very similar growth of  $\Gamma$  for all models. In fact, up to  $r \sim 10 - 50 r_{lc}$  the curves for models A2, C2 and D2 are almost identical. In model B2 the Lorentz factor increases somewhat more slowly. Further inspection reveals another anomaly of model B2 – in contrast to the C2 and D2 cases, where the highest Lorentz factor is found at the jet boundary, the fastest acceleration in the B2 solution occurs somewhat off the boundary. The reason for these anomalies is not clear but it may have something to do with the curvature of magnetic field lines – given the lower value of the power-law index  $a$ , model B2 retains a higher curvature at larger radii than models C2 and D2. The reason why the model D curve is significantly shorter than the other is that the strong collimation of the jet rapidly renders the computation prohibitively expensive in this case.

Since more rapidly collimated jets reach the same cylindrical radius at a larger distance from the source, the similar growth rates of the Lorentz factor with cylindrical radius imply a faster growth with spherical radius for less collimated jets. This is exactly what we see in the right panel of Fig. 10 – the conical jet of the A2 model reaches a Lorentz factor of 10 at a distance from the origin that is almost 100 times shorter than that of the paraboloidal jet of model C2.

Fig. 11 compares the magnitudes of the different magnetic field components in models A2–C2 near the far end of the jet ( $\eta = 10^3$ ). At this distance the jet radius is almost  $10^3$  larger than the light-cylinder radius and one would expect the azimuthal component of the magnetic field to dominate. Indeed, this is what is observed. On these scales the light

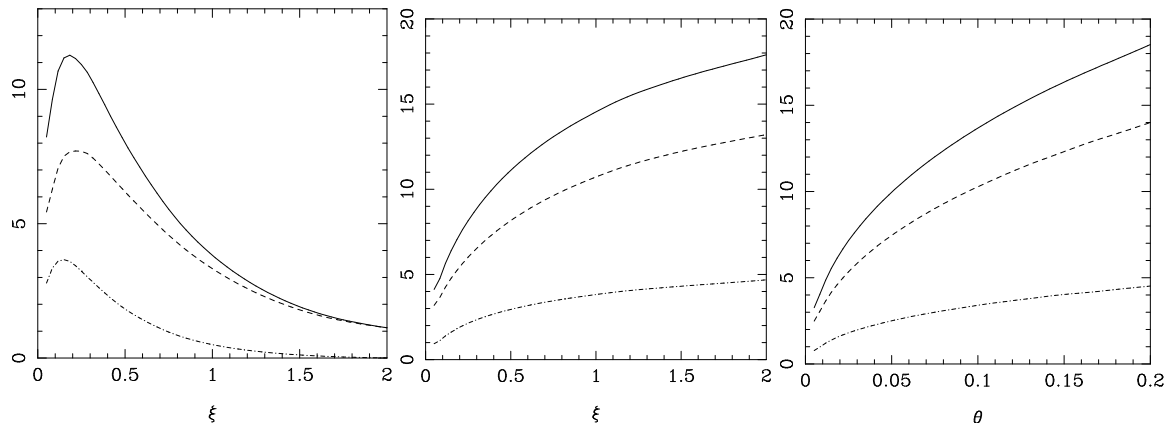


**Figure 9.** Distribution of  $\mu$  (solid line),  $\Gamma$  (dashed line) and  $\Gamma\sigma$  (dash-dotted line) across the jet for models C1 (left panel) and C2 (middle panel) at  $\eta = 10^5$ , and for model A2 (right panel) at  $\eta = 2 \times 10^3$ .

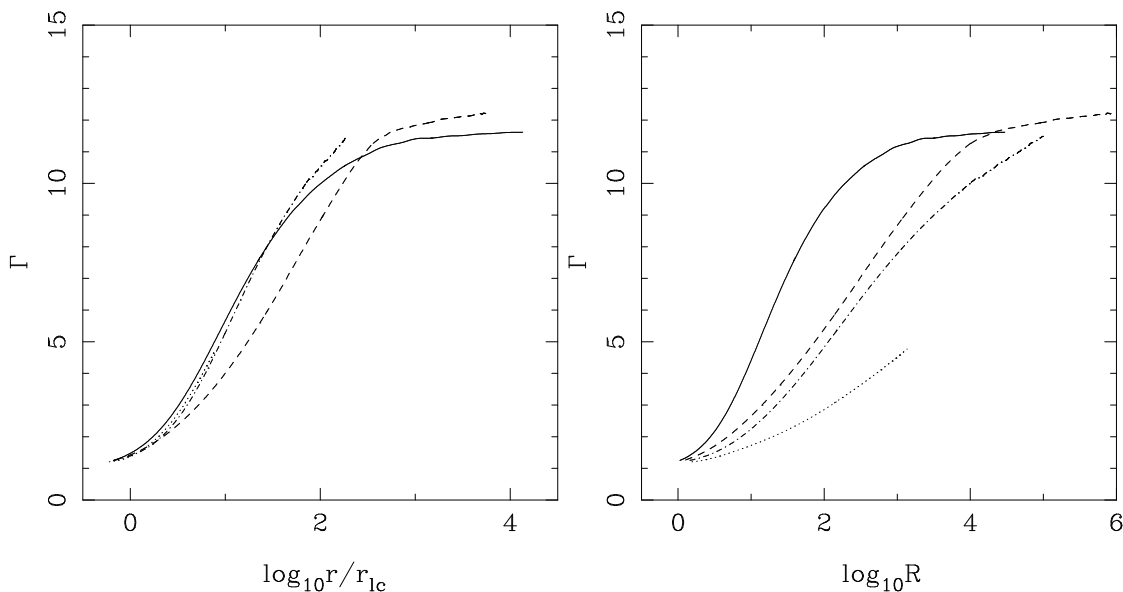


**Figure 10.** Lorentz factor along the jet boundary as a function of the cylindrical radius  $r$  (left panel) and the spherical radius  $R$  (right panel): model A2 – solid line; model B2 – dashed line; model C2 – dash-dotted line; model D2 – dotted line. Note that, although  $r_0$  and  $r_{1c}$  differ from model to model,  $R_0 = 1$  in all cases.

cylinder is no longer resolved on the computational grid, which explains why the azimuthal field component exceeds the poloidal components even near the symmetry axis. The fact that  $B^\phi$  does not vanish shows that the solution develops a core of high electric current density, and this core is also unresolved in our solution. The development of an axial line current in model C2 is shown in Fig. 5; very similar results are found also for the other models.

In an attempt to clarify the role of the imposed wall on the acceleration and collimation of the simulated jets, we performed additional simulations of model A2, corresponding to higher opening half-angles of the wall:  $\theta_c = 0.4, 0.8$ , and  $\pi/2$ , where the last case represents an unconfined outflow.<sup>7</sup> The results are presented in Figs. 12 and 13, which

should be compared with the corresponding plots in the right panels of Figs. 7–9. Not surprisingly, we find that the efficiency of magnetic acceleration is lower for weaker external collimation. This is particularly apparent in the unconfined case ( $\theta_c = \pi/2$ ), where the flow remains Poynting-dominated in the equatorial region of this distances. Nevertheless, even in the equatorial region of this extreme case the acceleration efficiency  $\Gamma_\infty/\mu$  is  $\sim 40\%$ . Furthermore, in the polar zone the efficiency is high, similarly to the small- $\theta_c$  case, with all models exhibiting a transition to the matter-dominated regime. In this sector self-collimation is strong as well (see Fig. 13). The behaviour of our unconfined jet model is consistent with the results of Li (1996), who showed (for both the nonrelativistic and modestly relativistic regimes) that a collimated axial jet can form from an initially spherical MHD wind. Those results were, however, derived on the assumption that the magnetic field is purely azimuthal and the velocity field purely poloidal from the start. The good collimation exhibited by all our jet models in the vicinity of

<sup>7</sup> Our original setup for this model corresponded to  $\theta_c = 0.2$ . We keep  $\Delta\theta$  (the cell size in the polar direction) the same for all models by increasing the number of cells for larger  $\theta_c$ .

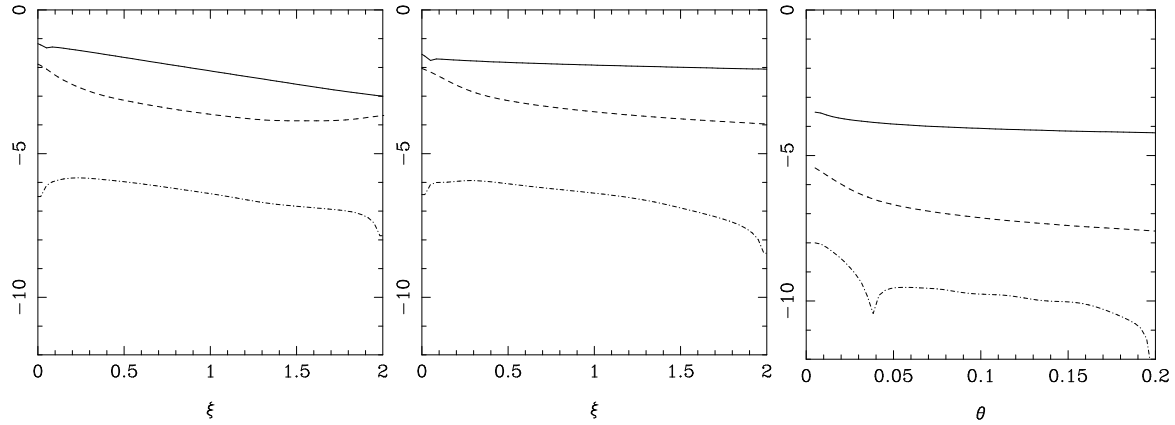


**Figure 11.** Variation of the magnetic field components across the jet at  $\eta = 6 \times 10^3$  in models C1 (left panel), C2 (middle panel) and A2 (right panel):  $\log_{10} |B^\phi|$  – solid line,  $\log_{10} B^\eta$  – dashed line,  $\log_{10} |B^\xi|$  – dash-dotted line.

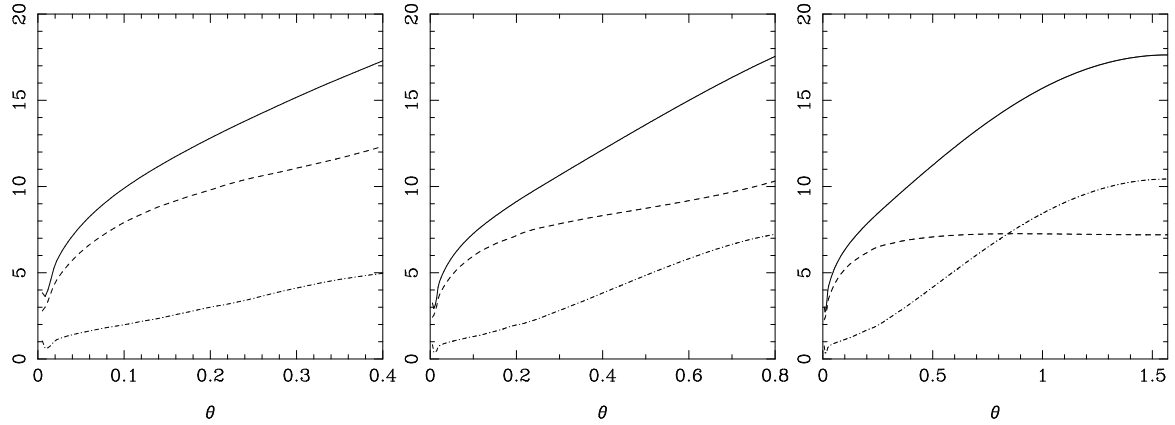


**Figure 12.** Distribution of  $\mu$  (solid line),  $\Gamma$  (dashed line) and  $\Gamma\sigma$  (dash-dotted line) across the jet for the cases of a conical boundary with an opening half-angle  $\theta_c = 0.4$  (left panel),  $0.8$  (middle panel), and  $\pi/2$  (right panel), an unconfined flow) at  $\eta = 2 \times 10^3$ . These are to be compared with the results for  $\theta_c = 0.2$  shown in the right panel of Fig. 9.

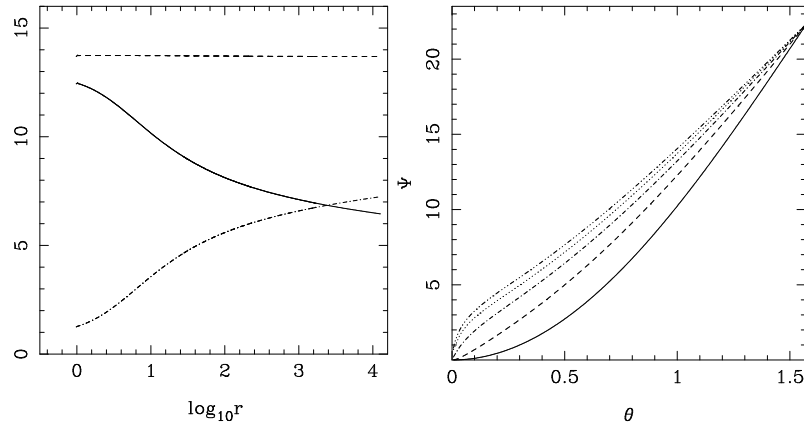


**Figure 13.** *Left panel:* Variation of  $\Gamma\sigma$  (solid line),  $\mu$  (dashed line) and  $\Gamma$  (dash-dotted line) along a magnetic field line for the case of a conical boundary with  $\theta_c = \pi/2$  (i.e. an unconfined flow). This is to be compared with the results for  $\theta_c = 0.2$  shown in the right panel of Fig. 8. *Right panel:* Evolution of the magnetic flux distribution across the jet. The solid line corresponds to  $\eta = 1$ , the dashed line to  $\eta = 30$ , the dash-dotted line to  $\eta = 3 \times 10^2$ , the dotted line to  $\eta = 3 \times 10^3$  and the dash-triply-dotted line to  $\eta = 3 \times 10^4$ . This is to be compared with the results for  $\theta_c = 0.2$  shown in the right panel of Fig. 7.

the axis can be attributed to the action of magnetic hoop stresses associated with a poloidal current flow, as discussed in § 5.1.

## 5 DISCUSSION

### 5.1 Theoretical aspects of the problem

Over the years there have been persistent doubts in the literature regarding the ability of magnetic forces to accelerate flows to relativistic speeds. In particular, several published studies have concluded that MHD acceleration of relativistic flows is inherently inefficient. This conclusion, however, is erroneous and can be attributed to the adoption of a conical (split-monopole) flow geometry in these studies. For example, in the work of Michel (1969) a simplified conical geometry was used in which the full system of relativistic MHD equations was not satisfied, whereas the results of Beskin et al. (1998) were based on a perturbative analysis around a quasi-conical flow. The conical flow geometry is unfavorable for acceleration for the following reason. Well outside the light cylinder, where  $r\Omega \gg v^{\hat{\phi}}$  and  $v \simeq c$ , equations (23) and (24) imply

$$rB^{\hat{\phi}} = -\frac{1}{c}\Omega B_p r^2. \quad (27)$$

From this equation and equation (16) one finds that

$$I = -\frac{1}{2}\Omega B_p r^2, \quad (28)$$

where  $B_p$  is the magnitude of the poloidal magnetic field. If the magnetic surfaces are conical then  $B_p \propto r^{-2}$ , and thus the poloidal electric current flows parallel to the magnetic field lines. In this case the component of the Lorentz force along the poloidal magnetic field lines,  $(1/c)\mathbf{j}_p \times \mathbf{B}_\phi$ , simply vanishes. More general treatments of the problem, based on exact semi-analytic solutions for axisymmetric, highly magnetized, steady outflows under the assumption of radial self-similarity (Li et al. 1992; Vlahakis & Königl 2003a,b, 2004), have demonstrated that magnetic acceleration in non-conical geometries can be quite efficient, typically resulting in a rough asymptotic equipartition between the Poynting and matter energy fluxes. A similar conclusion was reached on the basis of a perturbative analysis around a *parabolic* flow (Beskin & Nokhrina 2006). These results have indicated that the correct paradigm should, in fact, be that magnetic acceleration is generally a rather efficient mechanism for producing relativistic flows.

In this paper we have for the first time verified the proposed paradigm by means of numerical simulations of highly magnetized, relativistic flows. We have focused on the parameter regime that is most relevant to AGN jets. In a future paper (Komissarov et al., in preparation) we will present additional simulations that will demonstrate that this paradigm also applies to flows with terminal Lorentz factors that are as high as those inferred in gamma-ray burst sources.

One of the interesting outcomes of this study is the highly effective acceleration even in the case where the shape of the outer boundary is conical. Although the acceleration efficiency in conical steady flows is – as explained above – tiny, our results show that magnetic surfaces of conical jets

are not conical but rather paraboloidal (see Figs. 6 and 7), so  $B_p r^2$  is not constant. Fig. 14 shows the evolution of the function

$$\mathcal{S} = \frac{\pi r^2 B_p}{\Psi} = \frac{\pi r^2 B_p}{\int \mathbf{B}_p \cdot d\mathbf{S}} \quad (29)$$

along a typical magnetic surface for models C2 and A2. It is seen that in both cases  $\mathcal{S}$  undergoes a significant decrease with distance from the source. In fact, this decrease is faster in the conical-boundary model, which is reflected in the more rapid acceleration in this case (see Fig. 10). The direct relationship between the function  $\mathcal{S}$  and the acceleration efficiency can be readily shown by combining equations (17) and (28) to obtain

$$I\sigma = (\Psi\Omega^2/4\pi^2 kc^3)\mathcal{S} \propto \mathcal{S}.$$

Since  $\mathcal{S}$  depends on the shape of the flow, the latter relation brings out the importance of the trans-field force balance and the connection between acceleration and collimation. If the poloidal magnetic field is almost uniformly distributed across the jet then  $\mathcal{S} \sim 1$ ; this is the case near the inlet boundary. However, due to the collimation, the poloidal magnetic flux becomes concentrated near the rotation axis, forming a cylindrical core and causing  $\mathcal{S}$  to decrease with increasing  $r$  (see Fig. 15).

Our jet solutions are characterized by a high magnetic-to-kinetic energy conversion efficiency, but in the final states that we obtain the kinetic and Poynting energy fluxes are still of comparable magnitude, as previously found in the self-similar solutions (e.g. Vlahakis & Königl 2003a). We note in this connection that Begelman & Li (1994) conjectured on the basis of their asymptotic analysis that relativistic MHD outflows with a finite total magnetic flux will tend to convert their entire magnetic energy into kinetic energy at large distances from the origin. Although our solutions are terminated at a finite distance and thus we cannot exclude the possibility that eventually nearly all the magnetic energy will be extracted, it appears that this is unlikely to occur on astrophysically realistic scales. Furthermore, our discussion above suggests that the reason given by Begelman & Li (1994) for the limited conversion efficiency of self-similar flows, namely, that it may be hard to meaningfully decrease the quantity  $\pi r^2 B_p$  in a medium that contains an infinite magnetic flux  $\Psi$ , is not correct, since the relevant quantity is  $\mathcal{S} = \pi r^2 B_p / \Psi$  (equation 29), which remains finite even in the self-similar case.

Our results show efficient self-collimation, contrary to some claims in the literature and certain seemingly similar investigations that reached the opposite conclusion. As the term “self collimation” is sometimes misunderstood and confused with “self confinement”, we start by clarifying its meaning. In general, a hydromagnetic jet cannot be “self confined” for the simple reason that the “outward” effect of magnetic pressure always overcomes the “inward” effect of magnetic tension in MHD equilibria (see e.g. Section 5.3 in Parker 1979). There must always be an external medium that confines the system at its boundaries. (In our case the geometry of the wall translates into an effective ambient pressure distribution for any given flow problem; see Fig. 17 below.) It is, however, possible for a jet that carries an axial current to have the magnetic hoop stress collimate the innermost (current-carrying) streamlines relative to the

outer regions of the flow. This is what is generally meant by “self collimation.” The outer streamlines may or may not be collimated, depending on the global current flow and the confining pressure distribution (e.g. Begelman & Li 1994). The behaviour of the innermost streamlines is determined mostly by the axial current distribution. By showing that these streamlines collimate faster than the imposed boundary, we were able to demonstrate the action of the “self collimation” process in our jet models, including the limiting case of an unconfined flow (Fig. 13). The different cases that we examined served to illustrate how the transition from the inner region (small cylindrical radius  $R$ ) to the outer region (large  $R$ ) occurs for different effective confining pressure distributions.

Self-collimation in the super-Alfvénic regime of magnetized outflows is the result of the  $(1/c)\mathbf{j}_p \times \mathbf{B}_\phi$  force in the trans-field direction. In relativistic flows, the effect of this force is almost completely countered by the electric force, resulting in slower collimation compared to the nonrelativistic case (where the electric force is negligible). The asymptotic form of the trans-field equation in the highly relativistic limit is

$$\frac{\Gamma^2 r}{\mathcal{R}} \approx \left[ \frac{\left( \frac{2I}{\Omega B_p r^2} \right)^2 r \nabla \ln \left| \frac{I}{\Gamma} \right|}{1 + \frac{4\pi \rho u_p^2 r_{lc}^2}{B_p^2 r^2}} - \Gamma^2 \frac{r_{lc}^2}{r^2} \nabla r \right] \cdot \frac{\nabla \Psi}{|\nabla \Psi|} \quad (30)$$

(see equation 16 in Vlahakis 2004). From this equation it follows that the radius of curvature of poloidal field lines is  $\mathcal{R} \sim \Gamma^2 r$ . This fact led Tsinganos & Bogovalov (2002) to propose a two-component outflow model (central jet and surrounding disk wind) as a way of explaining the collimation of relativistic jets. However, as the self-similar solutions of Vlahakis & Königl (2004) as well as the present simulations show, self-collimation is still possible. In fact, it remains possible in flows with even higher asymptotic Lorentz factors (Vlahakis & Königl 2003a). Although for  $\Gamma \gg 1$  the collimation is indeed slow, it is more efficient near the source, where the flow is not yet highly relativistic.

Bogovalov (2001) solved a similar problem (using time-dependent equations near the central source and steady-state equations further out). Although the setup in that paper is similar to our case A2, the conclusions are different (inefficient collimation and therefore less efficient acceleration compared to our solution). There is, however, an important difference in the two setups. In Bogovalov’s (2001) paper the poloidal velocity at the inlet boundary is  $v_{p0} \approx 0.87c$ , corresponding to a Lorentz factor (including the azimuthal velocity) significantly higher than in our simulations. As explained above, a high Lorentz factor leads to a large  $\mathcal{R}/r$  ( $\sim \Gamma^2$ ). Another difference between the two works is that we are able to follow the flow to larger distances and hence to a smaller- $\sigma$  regime: in fact, in some cases (A2 and B2) our solutions extend all the way to the asymptotic regime, where the acceleration ceases and the Lorentz factor saturates to a constant value. Related to the above discussion is the fact that the mass and magnetic flux in our jet solutions are not “uncomfortably low” (as they were acknowledged to be in Bogovalov’s 2001 solution; see Tsinganos & Bogovalov

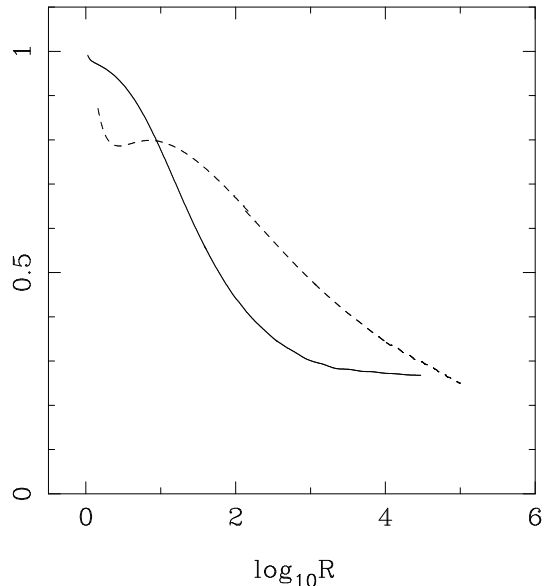


**Figure 14.** Evolution of the function  $\mathcal{S} = \pi B_p r^2 / \Psi$  along the magnetic surfaces of models A2 (solid line) and C2 (dashed line).

2002). In our solutions all the magnetic flux and all the outflowing mass are effectively collimated.<sup>8</sup>

The preceding discussion of the magnitude of the radius of curvature implicitly assumes that  $\mathcal{R}$  is positive. According to equation (30), the sign of  $\mathcal{R}$  depends on the sign of the three quantities  $\nabla |I| \cdot \nabla \Psi$ ,  $\nabla \Gamma \cdot \nabla \Psi$  and  $\nabla r \cdot \nabla \Psi$ . The term  $\nabla r \cdot \nabla \Psi$  always corresponds to decollimation and is important only in the matter-dominated flow regime far from the source (Vlahakis 2004). We can ignore this term in the main acceleration region where the flow is still magnetically dominated. The  $\mathbf{j}_p \cdot \mathbf{B}_p < 0$  current-carrying regime (in which  $\nabla |I| \cdot \nabla \Psi > 0$ ) contributes to positive  $\mathcal{R}$  and thus to collimation, whereas the return-current regime  $\mathbf{j}_p \cdot \mathbf{B}_p > 0$  promotes decollimation (Okamoto 2003). However, the sign of  $\mathcal{R}$  also depends on the gradient of  $\Gamma$ , a manifestation of the electric force. It is possible to have  $\mathcal{R} > 0$  even in the return-current regime provided that the Lorentz factor decreases with increasing cylindrical radius ( $\nabla \Gamma \cdot \nabla \Psi < 0$ ). In this case the electric force, which is directed toward the axis, dominates over the magnetic force, which points away from the axis, leading to collimation.<sup>9</sup> The net effect of the total electromagnetic force depends on the gradient of  $|I|/\Gamma$ , and collimation is possible if this quantity increases on moving across the field lines away from the polar axis (see also Li 1996). In agreement with this analysis, the positive value of  $\mathcal{R}$  in our models A1–D1 (which contain a current-carrying region near the axis and a return-current region near the outer boundary) requires the Lorentz factor to decrease with cylindrical radius (see e.g. Fig. 1). The decrease in  $\Gamma$  as the outer wall is approached is consistent (by equation 17) with

<sup>8</sup> The mass-loss rate between the axis and a particular field line  $\Psi = \text{const}$  is  $\dot{M} = 2 \int_0^\Psi k(\Psi) d\Psi$ . Since  $k(\Psi)$  is practically constant (see Fig. 4),  $\dot{M} \propto \Psi$  and the distribution of mass-loss rate across the jet can be deduced from the behaviour of  $\Psi(r)$  in Fig. 15.

<sup>9</sup> This behaviour was manifested also by the return-current self-similar solution presented in Vlahakis & Königl (2003a).



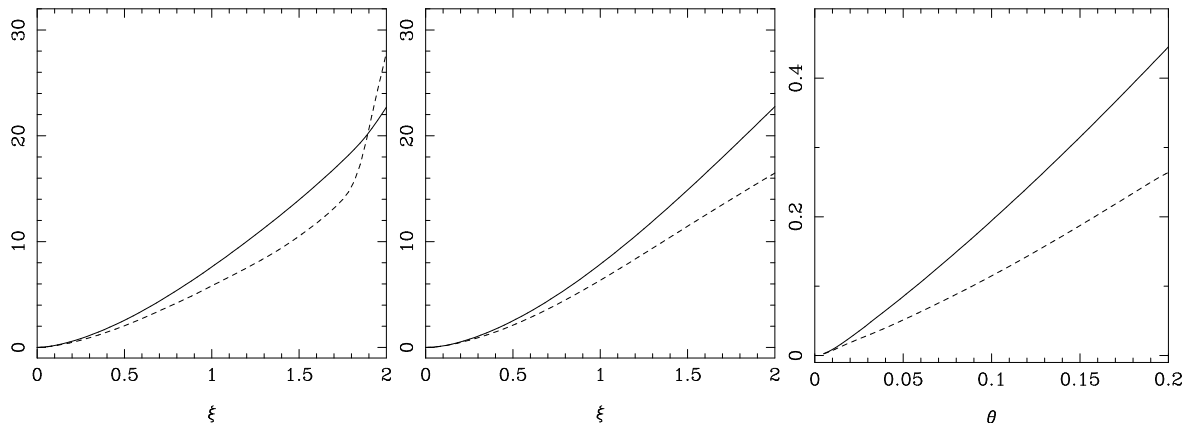


**Figure 15.** Variation of  $\Psi$  (solid line) and of  $r^2 B_p$  (dashed line) across the jet for models C1 (left panel), C2 (middle panel), and A2 (right panel) at  $z=30$ . Note that, for  $z = 30$ ,  $\xi = r/30^{1/a} \propto r$ . The plotted curves therefore make it possible to deduce the  $r$ -variation of the function  $S = \pi(r^2 B_p)/\Psi$  at a constant  $z$ .

the reduction in the electromagnetic acceleration brought about by the imposition of the boundary condition  $\Omega = 0$  at  $\xi = \xi_j$  (see equation 21).

To summarize the discussion on the collimation efficiency of relativistic jets, we have argued that collimation *is* possible in accelerating flows where the Lorentz factor ranges from  $\Gamma_0 \sim 1$  near the source to a high *asymptotic* (subscript  $\infty$ ) value  $\Gamma_\infty$ . Our choice of  $v_{p0}$  ( $= 0.5c$ ) at the inlet boundary and of the initial value of  $v^{\hat{r}}$  for the funnel plasma ( $= 0.7c$ ) allows the flow to relax to a collimated steady state with a high  $\Gamma_\infty$ . The sign of the curvature radius is positive even in the return-current regime because the Lorentz factor decreases sufficiently rapidly with  $r$  across the jet.

According to the asymptotic analysis of Heyvaerts & Norman (1989) and its relativistic generalization by Chiueh et al. (1991), the formation of a cylindrical core is the only way to have a non-singular current near the axis, i.e.  $I_\infty(\Psi = 0) = 0$ . Although our numerical results do not include the far-asymptotic state, the “solvability condition”  $I_\infty(\Psi)/\Gamma_\infty(\Psi) = \text{const}$  (a direct consequence of equation 30 in the limit  $r/\mathcal{R} \rightarrow 0^+$ ) is roughly satisfied; see Fig. 16.

The profile of  $\Omega(\xi)$  on the inlet boundary is used in our simulations as a proxy for the current distribution (see equation 28). However, in the cases A1–D1, where  $\Omega$  vanishes on the outer boundary,  $I$  nevertheless remains finite there. (Note that equation 28 holds only for  $r\Omega \gg v^{\hat{\phi}}$ , which is not satisfied when  $\Omega$  vanishes.) This is a reflection of a general property of ideal MHD flows: in the super-Alfvénic regime the azimuthal magnetic field cannot vanish<sup>10</sup> and the current lines close in a current sheet. In this respect our choice of an outer “wall” captures a basic physical aspect of a real boundary between a jet and an unmagnetized environment.

Since we have constructed our numerical jet models using time-dependent simulations, we have partly addressed the issue of stability to axisymmetric perturbations. Our

results indicate that, within our model setup, the jets are stable. Although the imposed solid outer boundary could have some stabilizing effect even on these modes, the extent of this influence is unclear, although in any case we do not expect the outer wall alone to prevent the growth of the pinch mode in the jet interior. Linear stability analyses of “Z-pinch” equilibria (magnetostatic cylindrical configurations with a weak uniform poloidal field and a strong toroidal field) have been used to argue that the kink mode would destroy the concentric configurations of astrophysical jets (Begelman 1998). While our simulations cannot address the possible effect of nonaxisymmetric modes, we nevertheless note that, in contrast to “Z-pinch” configurations, our jets show strong transverse gradients of poloidal velocity and magnetic field, which may be stabilizing factors (e.g. Anderson et al. 2006b).

## 5.2 Application to AGN Jets

The initial energy-to-mass flux ratio of jets in our simulations yields an upper limit on the terminal Lorentz factor  $\Gamma_\infty = \mu \leq 16$ . This is consistent with the mean values inferred in AGN jets (see Section 1). In order to make further comparisons of our numerical models with observations we need to select suitable dimensional scales. The key scale in the problem of magnetic acceleration is the light cylinder (or the Alfvén surface) radius,  $r_{lc}$ . If the jets are launched by a rapidly rotating black hole in the center of an AGN then

$$r_{lc} \simeq 4r_g = 6 \times 10^{13} (M/10^8 M_\odot) \text{ cm},$$

where  $r_g \equiv GM/c^2$ . In this estimate we assume that the angular velocity of the magnetic field lines is half of that of a maximally rotating (rotation parameter  $a \simeq 1.0$ ) black hole. According to the results shown in Fig. 8, the jets enter the matter-dominated regime, where an equipartition between Poynting and matter energy fluxes ( $\sigma \simeq 1$ ) is established, at a cylindrical radius

$$r_{eq} \simeq 30 r_{lc} \simeq 2 \times 10^{15} (M/10^8 M_\odot) \text{ cm},$$

<sup>10</sup> As explained in Vlahakis (2004), the invariance of  $B^2 - E^2$  yields  $B_\phi^2/B_p^2 > (r^2/r_{lc}^2) - 1$ . In highly magnetized flows the Alfvén surface almost coincides with the light surface, so  $(r^2/r_{lc}^2) - 1 > 0$  in the super-Alfvénic regime.

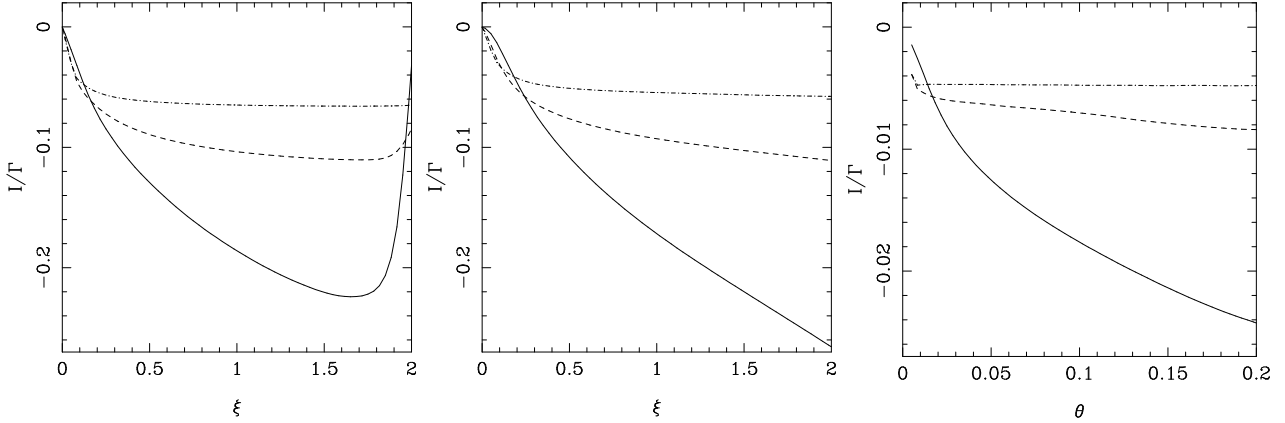


**Figure 16.** Distribution of  $I/\Gamma$  across the computed jets. *Left panel:* Model C1 at  $\eta = 80$  (solid line),  $\eta = 800$  (dashed line) and  $\eta = 8000$  (dash-dotted line); *Middle panel:* Model C2 at  $\eta = 80$  (solid line),  $\eta = 800$  (dashed line) and  $\eta = 8000$  (dash-dotted line); *Right panel:* Model A2 at  $\eta = 20$  (solid line),  $\eta = 200$  (dashed line) and  $\eta = 20000$  (dash-dotted line).

more or less independently of the details of jet collimation. The corresponding distance from the black hole is

$$R_{eq} \simeq 2 \times 10^{16} \left( \frac{M}{10^8 M_\odot} \right) \left( \frac{\Theta_j}{0.1} \right)^{-1} \text{ cm},$$

where  $\Theta_j$  is the jet opening half-angle. If blazar flux variability is associated with the propagation of strong shocks within the jet then we can expect this behaviour to originate on scales  $\gtrsim R_{eq}$ . When our simulated jets reach  $R \simeq 10 R_{eq}$ , their characteristic Lorentz factor becomes  $\sim 10$ . These properties of the extended magnetic acceleration region are in very good agreement with the observational inferences summarized in Section 1 (in particular, the lack of bulk-Comptonization spectral features in blazar jets; see Sikora et al. 2005).

Taking the characteristic initial radius poloidal magnetic field of a black hole-launched jet to be  $r_0 = r_g$  and  $B_0 = 10^5 \text{ G}$ , respectively, the mass-loss rate and total luminosity of the model jets scale as

$$\dot{M} = 10^{-2} \left( \frac{k\Psi}{0.2} \right) \left( \frac{B_0}{10^5 \text{ G}} \right)^2 \left( \frac{r_0}{r_g} \right)^2 \left( \frac{M}{10^8 M_\odot} \right)^2 M_\odot \text{ yr}^{-1}$$

and

$$\dot{\mathcal{E}} = 6 \times 10^{45} \left( \frac{\mu}{10} \right) \left( \frac{\dot{M}}{10^{-2} M_\odot \text{ yr}^{-1}} \right) \text{ ergs s}^{-1},$$

respectively, where  $k$ ,  $\Psi$  and  $\mu$  are the mean values of the dimensionless flow constants shown in Fig. 4.

From the theory of black-hole magnetospheres (e.g. Blandford & Znajek 1977) it follows that, at their base, black-hole jets are highly magnetically dominated, so that the energy per particle greatly exceeds the Lorentz factor inferred from observations of AGN jets. This difficulty can be overcome if there are other ways of injecting particles into AGN jets in addition to pair cascades. It is conceivable that a sufficient supply of particles is provided by the winds of stars that lie in the paths of the jets as they make their way out of the galactic nuclei (e.g. Komissarov 1994; Hubbard & Blackman 2006). In fact, the injection rate could be high enough to explain the observed deceleration of weak FR-I jets down to subrelativistic speeds. In addition some mass is unavoidably entrained through the interface between

the jet and the confining external medium via diffusive processes. Another possibility is that the speed of AGN jets is controlled by the dissipation at oblique shocks developing as a result of an interaction with an unsteady external flow or due to various instabilities (McKinney 2006). Compton-drag interaction with the ambient radiation field may also be a factor (e.g. Melia & Königl 1989).

The problem of low initial mass loading might be circumvented if the bulk of the relativistic outflow component in fact originates in the nuclear accretion disk (see, e.g. Ghosh & Abramowicz 1997; Livio et al. 1999), which is the scenario adopted in the semi-analytic models of Vlahakis & Königl (2004). Although the chosen distributions of angular velocity, magnetic field and density at the inlet boundary do not formally match a Keplerian disk, our solutions can be interpreted in the context of disk-driven outflows. Taking  $\Omega_K(r_0)$  to be the Keplerian angular velocity at the reference distance  $r_0$ , we find that

$$r_{lc} = 5 \times 10^{14} \left( \frac{M}{10^8 M_\odot} \right) \left( \frac{r_0}{10 r_g} \right)^{3/2} \left[ \frac{\Omega_K(r_0)}{\Omega} \right] \text{ cm}$$

and that  $\sigma \approx 1$  is reached at a distance

$$R_{eq} \simeq 10^{17} \left( \frac{r_{lc}}{5 \times 10^{14} \text{ cm}} \right) \left( \frac{\Theta_j}{0.1} \right)^{-1} \text{ cm}.$$

The mass-loss rate and jet power are

$$\dot{M} = 10^{-2} \left( \frac{k\Psi}{0.2} \right) \left( \frac{B_0}{10^4 \text{ G}} \right)^2 \left( \frac{r_0}{10 r_g} \right)^2 \left( \frac{M}{10^8 M_\odot} \right)^2 M_\odot \text{ yr}^{-1}$$

and

$$\dot{\mathcal{E}} = 6 \times 10^{45} \left( \frac{\mu}{10} \right) \left( \frac{\dot{M}}{10^{-2} M_\odot \text{ yr}^{-1}} \right) \text{ ergs s}^{-1},$$

respectively. The striking differences in the velocity profile between simulated jets with solid-body rotation and with differential rotation (see Figs. 1 and 2 for models C1 and C2, respectively) suggests (taking into account relativistic beaming effects) that it might be possible to distinguish between jets launched directly from a black hole and those that emanate from the surface of an accretion disk in cases where the transverse structure of the jet can be resolved. One would, however, need to verify that these differences

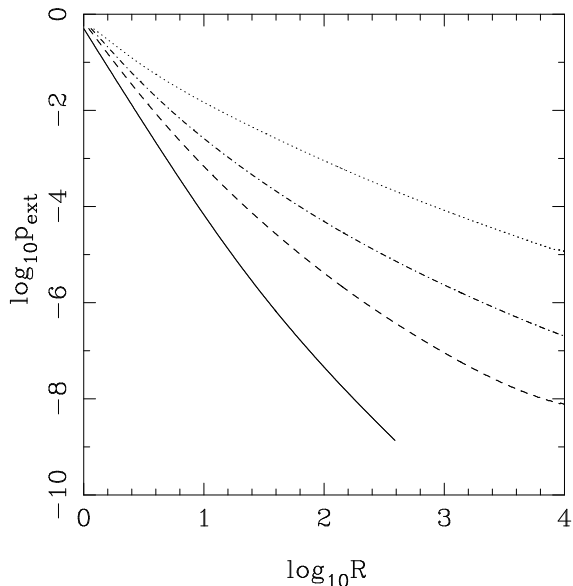


**Figure 17.** Ambient pressure distribution required for the collimation of the computed jets. Model A2 – solid line; model B2 – dashed line; model C2 – dash-dotted line; model D2 – dotted line.

remain noticeable for more realistic disk rotation laws and surface field distributions.

The funnel shapes in our simulations were chosen merely for the purpose of studying the effects of overall flow collimation on its magnetic acceleration. However, from our steady-state solutions we can infer the effective external force (normal to the jet surface) that is required to provide the collimation imposed by our choice of the outer-boundary shape. AGN jets could be confined by a variety of forces, including, for example, the thermal pressure of an ambient gas distribution, the ram pressure of a wind from the outer regions of the nuclear disk, and the stress of a magnetic field anchored in the disk (and possibly embedded in a disk outflow). Fig. 17 shows the effective pressure deduced in this way ( $p_{\text{ext}} = b^2/8\pi$ ) as a function of spherical radius for models A2–D2. Although none of the curves is an exact power law of the form  $p_{\text{ext}} \propto R^{-\alpha}$ , it is nevertheless informative to calculate mean power-law indices. We find  $\alpha \approx 3.5, 2, 1.6$  and  $1.1$  for models A2, B2, C2 and D2, respectively. The models are thus seen to cover a wide range of behaviours. As expected, the more highly collimated funnel geometries correspond to the less steeply declining effective pressure distributions. The largest indices might correspond to confinement by a wind. For example, in a spherical wind of polytropic index  $5/3$ , the thermal pressure scales as  $R^{-10/3}$  and the ram pressure as  $R^{-5/2}$ . Thus, a disk wind that assumes a nearly spherical geometry as it propagates away from the disk surface could effectively confine a relativistic jet with a nearly conical outer boundary. We note in this connection that Begelman & Li (1994) suggested that collimated jets necessarily correspond to confining pressure distributions with  $\alpha \lesssim 2$ . Our results indicate that higher values of the effective power-law index are also possible.

Although we have focused in this paper on AGN jets, it is interesting to note that relativistic outflows with terminal Lorentz factors as high as  $\sim 10$  have also been inferred in

Galactic X-ray binary sources, which comprise both black holes and neutron stars (e.g. Fender et al. 2004), and that arguments have been advanced in support of the possibility that the mean Lorentz factors in these sources are comparable to those estimated in AGNs (Miller-Jones et al. 2006)). The magnetic acceleration mechanism discussed in this paper is also a likely candidate for the driving of X-ray binary jets (e.g. Livio et al. 2003). However, even if these jets are similar to those in AGNs, as of now the latter remain the best targets for observations that could test and constrain the model.

## 6 CONCLUSION

This paper presents the results of special-relativistic, ideal-MHD numerical simulations of AGN jets. The numerical code employed in these simulations was specifically designed for this task. In contrast to most previous numerical schemes that modeled relativistic MHD jets, our code does not require a large artificial viscosity for numerical stability and is well suited for studies of two-dimensional stationary flows that are aligned with the computational grid. To avoid numerical dissipation induced at the interface with an ambient medium, we have simplified the calculation by taking the flow to be confined by a solid wall. We took the shape of the wall to be either a paraboloid of revolution or a cone and used corresponding elliptical or spherical coordinates to optimize the resolution as well as the alignment of the flow with the computational grid. In addition, we implemented a grid-extension method that allowed us to follow the flow out to scales  $\sim 10^4 - 10^6$  times that of the inlet boundary, which was crucial to our ability to study the inherently extended nature of MHD acceleration to high Lorentz factors. To ensure the self-consistency of this procedure, we derived the condition for the Mach cone of the fast-magnetosonic waves to point outward at the boundary between a given grid sector and the successive one, and we verified that this condition is satisfied at each of the relevant sector interfaces.

Our carefully designed numerical scheme has enabled us to simulate, for the first time, the magnetic acceleration and collimation of relativistic jets to completion. In particular, we have found that initially Poynting flux-dominated jets can be effectively accelerated to high bulk Lorentz factors with an efficiency (defined as the ratio of the final kinetic energy flux to the total energy flux)  $\gtrsim 50\%$ . As expected from previous semi-analytic (radially self-similar) solutions for steady-state flows, the acceleration process is spatially extended. We have found that our simulated jets invariably settle to a steady state, which suggests (although we did not explore this issue explicitly) that the resulting flow configurations are not inherently unstable (at least not to axisymmetric perturbations – although it is conceivable that the imposed rigid wall has a stabilizing influence in this regard – and excluding by design any effects of a direct interaction with an ambient medium). The properties of the derived final configurations were found to be qualitatively very similar to those of the self-similar AGN jet solutions of Vlahakis & Königl (2004) and to not depend sensitively on either the imposed shape of the outer boundary or on the distribution of the injected poloidal current at the inlet boundary. (We explored boundaries with scalings, in cylin-

dical coordinates, ranging from  $z \propto r$  to  $z \propto r^3$ , and current distributions that either closed within the volume of the jet or on its outer boundary.)

We provided a physical explanation of the basic acceleration process and of the variations in the detailed behaviour among the different flow configurations that we simulated. We argued that the robustness of the acceleration process can be attributed to the fact that the bulk of the outflow initially follows paraboloidal trajectories, including the case of a conical outer boundary. We highlighted the connection between the collimation of the flow, which is manifested in the curved streamlines, and the acceleration process. The collimation in the current-carrying regime is essentially due to magnetic hoop stress associated with the azimuthal magnetic-field component  $B_\phi$ . The collimation induces a reduction in the magnitude of  $r^2 B_p$  (where  $B_p$  is the poloidal field component) along the poloidal streamlines, which corresponds to a decrease in the Poynting flux along the flow and therefore results in acceleration (driven by the gradient of the magnetic pressure associated with  $B_\phi$ ). Previous claims in the literature that magnetic acceleration of relativistic flows is inefficient were all based on the assumption that the streamlines have a split-monopole geometry (or very nearly so), which is a singular case in which by fiat  $r^2 B_p$  remains constant (or close to a constant) along the flow.

Our solutions also revealed that the collimation efficiency of relativistic jets can be high if they are accelerated from an initial Lorentz factor  $\Gamma_0 \sim 1$ . We argued that published results in the literature that claimed otherwise in fact had a significantly higher  $\Gamma_0$ . Once the flow attains a high Lorentz factor the collimation process slows down on account of the increased inertia and of the growth of the electric force, which almost completely balances the transverse magnetic force. Nevertheless, the current-carrying central region of our simulated jets collimates much faster than the imposed boundaries and attains a cylindrical shape by the time the terminal Lorentz factor is attained, again in full agreement with the semi-analytic self-similar solutions (which also assumed  $\Gamma_0 \sim 1$ ). In simulated outflows where the current returns through the jet we found that the flow is effectively collimated also in the outer, return-current region (in this case by the electric force, which dominates the transverse magnetic force that acts to decollimate the flow in this regime). The efficient electromagnetic collimation in all of our computed jet models is evidently the reason why the presence of a rigid outer boundary does not induce recollimation shocks in the outflow even for the most rapidly converging wall shape ( $r \propto z^3$ ).

In validating the basic features of the simplified semi-analytic solutions, our numerical results go a long way toward establishing an ‘‘MHD acceleration and collimation paradigm’’ for relativistic astrophysical jets. In this contribution we applied this model to AGN jets, for which there is already significant observational evidence of extended,  $\gtrsim 0.1$  pc-scale acceleration (possibly continuing to  $\sim 1 - 10$  pc) to Lorentz factors  $\gtrsim 10$ . We demonstrated that, for plausible physical parameters, our simulated jets can reproduce these observations (see also Vlahakis & Königl 2004). We noted that these results could potentially apply also to the jets observed in Galactic X-ray binary sources. In a future publication we will present simulation results

for even higher initial magnetizations that could be used to model the ultrarelativistic jets in gamma-ray burst sources.

Future investigations will need to examine some of the complicating factors left out of the present study. In particular, the simplifying wall boundary condition will have to be replaced by the interaction of the outflow with its environment. Furthermore, the questions of stability and energy dissipation will have to be addressed. In fact, given the potentially destructive role of the kink mode, fully 3D relativistic simulations will ultimately need to be carried out. In addition, the response of the jet to nonsteady conditions at the source – a potential cause of observed variability – will be an interesting topic for study.

## ACKNOWLEDGMENTS

We thank Mitch Begelman and Anatoly Spitkovsky for helpful comments and Jonathan McKinney for useful correspondence. We also acknowledge extensive suggestions by the referee. This research was funded by PPARC under the rolling grant ‘‘Theoretical Astrophysics in Leeds’’ (SSK and MVB). NV acknowledges partial support by the European Social Fund and National Resources – (EPEAEK II) PYTHAGORAS. AK was partially supported by a NASA Theoretical Astrophysics Program grant.

## APPENDIX A: ELLIPTIC COORDINATES

We assume that the jet boundary satisfies the power law

$$z \propto r^a, \quad (\text{A1})$$

where  $\{r, z\}$  are cylindrical coordinates. Then the condition that the jet boundary be a coordinate surface suggests we choose

$$\xi = rz^{-1/a} \quad (\text{A2})$$

as one of the spatial coordinates. The other coordinate,  $\eta$ , is defined in such a way that the coordinate system becomes orthogonal. The orthogonality condition

$$\nabla\xi \cdot \nabla\eta = 0 \quad (\text{A3})$$

leads to a PDE for  $\eta$ ,

$$\frac{\partial\eta}{\partial r} - \frac{1}{a} \frac{r}{z} \frac{\partial\eta}{\partial z} = 0, \quad (\text{A4})$$

which allows separable solutions. The requirement  $\eta = 0$  for  $(r, z) = (0, 0)$  leads to

$$\eta^2 = \frac{r^2}{a} + z^2. \quad (\text{A5})$$

Thus, the  $\eta$  coordinate lines are ellipses with semi-axes  $\eta$  and  $\sqrt{a}\eta$ . The remaining spatial coordinate is the usual azimuthal angle  $\phi$ .

Conversion from elliptical to cylindrical coordinates involves solving a transcendental equation for  $z$ :

$$z^2 + \frac{\xi^2}{a} z^{2/a} - \eta^2 = 0. \quad (\text{A6})$$

In the general case this equation has no analytic solutions, but for certain values of the power-law index  $a$  it reduces to simpler equations:

$$a = 3/2, \quad y^3 + \frac{2}{3}\xi^2 y^2 - \eta^2 = 0, \quad \text{where } y = z^{3/2}; \quad (\text{A7})$$

$$a = 1, \quad z^2 + \xi^2 z^2 - \eta^2 = 0; \quad (\text{A8})$$

$$a = 2, \quad z^2 + \frac{\xi^2}{2}z - \eta^2 = 0; \quad (\text{A9})$$

$$a = 3, \quad y^3 + \frac{\xi^2}{3}y - \eta^2 = 0, \quad \text{where } y = z^{2/3}. \quad (\text{A10})$$

The metric tensor in these coordinates is diagonal with components

$$g_{\xi\xi} = \frac{a^2 z^{2(1+a)/a}}{D}, \quad (\text{A11})$$

$$g_{\eta\eta} = \frac{a^2 \eta^2}{D}, \quad (\text{A12})$$

$$g_{\phi\phi} = r^2, \quad (\text{A13})$$

$$g_{tt} = -1, \quad (\text{A14})$$

where  $D = a^2 z^2 + r^2$ . Its determinant is

$$g = -\frac{a^4 r^2 \eta^2 z^{2(1+a)/a}}{D^2}. \quad (\text{A15})$$

The non-vanishing derivatives of these components are

$$g_{\xi\xi,\xi} = -\frac{1}{D^3} 2a^2 r z^{(3+2a)/a} [2a^2 z^2 + r^2(1+a)], \quad (\text{A16})$$

$$g_{\xi\xi,\eta} = \frac{1}{D^3} 2a^5 \eta^3 z^{(2+2a)/a}, \quad (\text{A17})$$

$$g_{\eta\eta,\xi} = \frac{1}{D^3} 2a^4 (a-1) r z^{(1+2a)/a} \eta^2, \quad (\text{A18})$$

$$g_{\eta\eta,\eta} = -\frac{1}{D^3} 2a^3 (a-1)^2 r^2 z^2 \eta, \quad (\text{A19})$$

$$g_{\phi\phi,\xi} = \frac{1}{D} 2a^2 r z^{(1+2a)/a}, \quad (\text{A20})$$

$$g_{\phi\phi,\eta} = \frac{1}{D} 2ar^2 \eta. \quad (\text{A21})$$

## APPENDIX B: FAST MAGNETOSONIC WAVES

Suppose that we study an axisymmetric magnetosonic disturbance whose wavevector is

$$\mathbf{k} = k \left( \frac{\mathbf{v}_p}{v_p} \cos \vartheta_k + \hat{\phi} \times \frac{\mathbf{v}_p}{v_p} \sin \vartheta_k \right). \quad (\text{B1})$$

Its frequency is  $\omega = k\mathcal{P}(\vartheta_k)$ , with  $\mathcal{P}$  satisfying

$$\begin{aligned} & \frac{B_p^2 c_s^2}{4\pi w/c^2} \left[ \cos^2 \vartheta_k - \left( \frac{r}{r_{lc}} \cos \vartheta_k + \frac{\mathcal{P}}{c} \frac{B_\phi}{B_p} \right)^2 - \frac{\mathcal{P}^2}{c^2} \right] \\ & - (\Gamma\mathcal{P} - u_p \cos \vartheta_k)^2 \left[ \frac{B^2 - E^2}{4\pi w/c^2} \left( 1 - \frac{c_s^2}{c^2} \right) + c_s^2 \right] \\ & + \frac{(\Gamma\mathcal{P} - u_p \cos \vartheta_k)^4}{1 - \mathcal{P}^2/c^2} \left( 1 - \frac{c_s^2}{c^2} \right) = 0 \end{aligned} \quad (\text{B2})$$

(see Appendix C in Vlahakis & Königl 2003a). The disturbance travels with a group velocity

$$\mathbf{v}_g = \nabla_{\mathbf{k}} \omega = \frac{\mathbf{k}}{k} \mathcal{P} + \hat{\phi} \times \frac{\mathbf{k}}{k} \mathcal{P}', \quad (\text{B3})$$

where  $\mathcal{P}' \equiv d\mathcal{P}/d\vartheta_k$ . The group velocity makes an angle  $\vartheta_g$  with respect to the poloidal flow velocity, where

$$\tan \vartheta_g = \frac{\mathbf{v}_g \cdot \hat{\phi} \times \mathbf{v}_p}{\mathbf{v}_g \cdot \mathbf{v}_p} = \frac{\mathcal{P} \sin \vartheta_k + \mathcal{P}' \cos \vartheta_k}{\mathcal{P} \cos \vartheta_k - \mathcal{P}' \sin \vartheta_k}. \quad (\text{B4})$$

The envelope of the family of such disturbances (whose trajectories are defined by the angle  $\vartheta_k$ ) constitutes the Mach cone of fast-magnetosonic waves at any given point in the flow. It is given by combining equation (B4) and the condition

$$\frac{d}{d\vartheta_k} \left( \frac{\mathcal{P} \sin \vartheta_k + \mathcal{P}' \cos \vartheta_k}{\mathcal{P} \cos \vartheta_k - \mathcal{P}' \sin \vartheta_k} \right) = 0. \quad (\text{B5})$$

After some manipulation, equation B5 yields  $\mathcal{P} = 0$ .<sup>11</sup> Thus, the fast Mach cone corresponds to a particular combination ( $\vartheta_k, \vartheta_g$ ) of the angles  $\vartheta_k$  and  $\vartheta_g$  that satisfies  $\tan \tilde{\vartheta}_g = -\cot \vartheta_k$  and  $\mathcal{P}(\tilde{\vartheta}_k) = 0$ . Using equation (B2), these conditions yield

$$\frac{B^2 - E^2}{4\pi w/c^2} + \frac{c_s^2}{1 - c_s^2/c^2} \left[ 1 - \frac{B_p^2/u_p^2}{4\pi w/c^2} \left( 1 - \frac{r^2}{r_{lc}^2} \right) \right] \sin^2 \tilde{\vartheta}_g = \frac{u_p^2}{u_p^2}. \quad (\text{B6})$$

The requirement that the Mach cone points outward at a surface  $\eta = \text{const}$  is that the angle  $\arcsin[|\hat{\eta} \cdot \mathbf{v}_p/v_p|]$  between the surface and the poloidal flow velocity exceeds  $\tilde{\vartheta}_g$ , or  $|\hat{\eta} \cdot \mathbf{v}_p/v_p|^2 > \sin^2 \tilde{\vartheta}_g$ . Using equation (B6) and  $B_p/v_p = B^{\tilde{\eta}}/v^{\tilde{\eta}}$ , this last inequality can be transformed into equation (25).

## REFERENCES

- Anderson M., Hirschmann E. W., Liebling S. L., Neilsen D., 2006a, CQGra, 23, 6503  
 Anderson J. M., Li Z.-Y., Krasnopolsky R., Blandford R. D., 2006b, ApJ, 653, L33  
 Anninos P., Fragile P. C., Salmonson J. D., 2005, ApJ, 635, 723  
 Antón L., Zanotti O., Miralles J. A., Martí J. M., Ibáñez J. M., Font J. A., Pons J. A., 2006, ApJ, 637, 296  
 Bach U., Krichbaum T. P., Kraus A., Witzel A., Zensus J. A., 2006, A&A, 452, 83  
 Begelman M. C., Blandford R. D., Rees M. J. Reviews of Modern Physics, 1984, 56, 255  
 Begelman M. C., 1998, ApJ, 493, 291  
 Begelman M. C., Li Z.-Y., 1994, ApJ, 326, 269  
 Beskin V. S., Kuznetsova I. V., Rafikov R. R., 1998, MNRAS, 299, 341  
 Beskin V. S., Nokhrina E. E., 2006, MNRAS, 367, 375  
 Blandford R. D., 1976, MNRAS, 176, 465  
 Blandford R. D., 2002, in Gilfanov M., Sunyaev R., Churazov E., eds, Lighthouses of the Universe. Springer, Berlin, p. 381  
 Blandford R. D., Payne D. G., 1982, MNRAS, 199, 883  
 Blandford R. D., Rees M. J., 1974, MNRAS, 169, 395  
 Blandford R. D., Znajek R. L., 1977, MNRAS, 179, 433  
 Bogovalov S. V., 1997, A&A, 323, 634  
 Bogovalov S. V., 2001, A&A, 371, 1155

<sup>11</sup> The other solution of equation (B5),  $\mathcal{P}'' + \mathcal{P} = 0$ , is related to the propagation of slow-magnetosonic waves; see Vlahakis (1998).

- Camenzind M., 1989, in Belvedere G., ed., *Accretion Disks and Magnetic Fields in Astrophysics*. Kluwer, Dordrecht, p. 129
- Chiueh T., Li Z.-Y., Begelman M. C., 1991, *ApJ*, 377, 462
- Cohen M. H., Lister M. L., Homan D. C., Kadler M., Kellermann K. I., Kovalev Y. Y., Vermeulen R. C., 2007, *ApJ*, 658, 232
- Contopoulos J., 1994, *ApJ*, 432, 508
- Del Zanna L., Bucciantini N., Londrillo P., 2003, *A&A*, 400, 397
- De Villiers J.-P., Hawley J. F., Krolik J. H., Hirose S., 2005, *ApJ*, 620, 878
- Drenkhahn G., Spruit H. C., 2002, *A&A*, 391, 1141
- Duez M. D., Liu Y. T., Shapiro S. L., Stephens B. C., 2005, *Phys. Rev. D*, 72, 024028
- Fender R., Wu K., Johnston H., Tzioumis T., Jonker P., Spencer R., van der Klis M., 2004, *Nature*, 427, 222
- Gammie C. F., McKinney J. C., Toth G., 2003, *ApJ*, 589, 444.
- Georganopoulos M., Kazanas D., 2003, *ApJ*, 589, L5
- Ghosh P., Abramowicz M. A., 1997, *MNRAS*, 292, 887
- Hartman R. C. et al., 2001, *ApJ*, 553, 683
- Heyvaerts J., Norman C., 1989, *ApJ*, 347, 1055
- Homan D. C., Ojha R., Wardle J. F. C., Roberts D. H., Aller M. F., Aller H. D., Hughes P. A., 2001, *ApJ*, 549, 840
- Hubbard A., Blackman E. G., 2006, *MNRAS*, 371, 1717
- Jorstad S. G. et al., 2005, *AJ*, 130, 1418
- Jorstad S. G., Marscher A. P., Mattox J. R., Wehrle A. E., Bloom S. D., Yurchenko A. V., 2001, *ApJS*, 134, 181
- Koide S., Shibata K., Kudoh T., 1999, *ApJ*, 522, 727
- Komissarov S. S., 1994, *MNRAS*, 266, 649
- Komissarov S. S., 1999, *MNRAS*, 303, 343
- Komissarov S. S., 2002, *MNRAS*, 350, 1431
- Komissarov S. S., 2004, *MNRAS*, 350, 1431
- Komissarov S. S., 2006, *AIPC*, 856, 129
- Komissarov S. S., Lyubarsky Y. E., 2004, *MNRAS*, 349, 779
- Komissarov S. S., Barkov M., Lyutikov M., 2007, *MNRAS*, 374, 415
- Königl A., 1982, *ApJ*, 261, 115
- Li Z.-Y., 1996, *ApJ*, 473, 873
- Li Z.-Y., Chiueh T., Begelman M. C., 1992, *ApJ*, 394, 459
- Livio M., Ogilvie G. I., Pringle J. E., *ApJ*, 512, 100
- Livio M., Pringle J. E., King A. R., 2003, *ApJ*, 593, 184
- Lobanov A. P., Roland J., 2005, *A&A*, 431, 831
- Lobanov A. P., Zensus J. A., 1999, *ApJ*, 521, 509
- Lovelace R. V. E., 1976, *Nature*, 262, 649
- Lyutikov M., Blandford R. D., 2003, preprint (astro-ph/0312347)
- McKinney J. C., 2006, *MNRAS*, 368, 1561
- McKinney J. C., Gammie C. F. 2004, *ApJ*, 611, 977
- Melia F., Königl A., 1989, *ApJ*, 340, 162
- Michel F. C., 1969, *ApJ*, 158, 727
- Miller-Jones J. C. A., Fender R. P., Nakar E., 2006, *MNRAS*, 367, 1432
- Narayan R., McKinney J. C., Farmer A. J., 2007, *MNRAS*, 375, 548
- Okamoto I., 2003, *ApJ*, 589, 671
- Parker E. N., 1979, *Cosmical Magnetic Fields*. Clarendon, Oxford
- Piner B. G., Unwin S. C., Wehrle A. E., Zook A. C., Urry C. M., Gilmore D. M., 2003, *ApJ*, 588, 716
- Rebillot P. F. et al., 2006, *ApJ*, 641, 740
- Shibata M., Sekuguchi Y. I., 2005, *Phys. Rev. D.*, 72, 044014
- Shu F. H., Najita J., Ostriker E. C., Shang H., 1995, *ApJ*, 455, L155
- Sikora M., Begelman M. C., Madejski G. M., Lasota J.-P., 2005, *ApJ*, 625, 72
- Tsinganos K., Bogovalov S., 2002, *MNRAS*, 337, 553
- Unwin S. C., Wehrle A. E., Lobanov A. P., A. Z. J., Madejski G. M., Aller M. F., 1997, *ApJ*, 480, 596
- Villata M. et al., 2006, *A&A*, 453, 817
- Vlahakis N., 1998, Ph.D. Thesis, Univ. Crete, p. 64
- Vlahakis N., 2004, *ApJ*, 600, 324
- Vlahakis N., Königl A., 2003a, *ApJ*, 596, 1080
- Vlahakis N., Königl A., 2003b, *ApJ*, 596, 1104
- Vlahakis N., Königl A., 2004, *ApJ*, 605, 656
- Vlahakis N., Tsinganos K., Sauty C., Trussoni E., 2000, *MNRAS*, 318, 417
- Walker R. C., Benson J. M., Unwin S. C., Lystrup M. B., Hunter T. R., Pilbratt G., Hardee P. E., 2001, *ApJ*, 556, 756